



Determination of flow regimes and heat transfer coefficient for condensation in horizontal tubes



Ilchung Park, Hyoungsoon Lee, Issam Mudawar*

Purdue University Boiling and Two-Phase Flow Laboratory (PU-BTFL), Mechanical Engineering Building, 585 Purdue Mall, West Lafayette, IN 47907-2088, USA

ARTICLE INFO

Article history:

Received 8 April 2014

Received in revised form 16 September 2014

Accepted 16 September 2014

Available online 17 October 2014

Keywords:

Condensation
Horizontal flow
Regime maps
Annular flow

ABSTRACT

This study explores condensation of FC-72 in horizontal tubes. Using high-speed video motion analysis, dominant condensation flow regimes are identified for different combination of mass velocities of FC-72 and cooling water. Additionally, detailed heat transfer measurements are used to explore both axial and circumferential variations of the condensation heat transfer coefficient. Four different regimes are identified: *stratified*, *stratified-wavy*, *wavy-annular with gravity influence*, and *wavy-annular without gravity influence*. In the latter regime, which is achieved at high FC-72 mass velocities, annular film transport is dominated by vapor shear with negligible gravity effects. Using different types of regime maps, prior relations for transitions between regimes are assessed, and new, more accurate transition relations developed. The heat transfer coefficient is shown to be highest near the inlet, where quality is near unity and the film thinnest, and decreases gradually along the condensation length because of axial thickening of the liquid film. This study also explores the predictive capabilities of prior heat transfer correlations and a control-volume-based annular flow model. The experimental data of both the local and average condensation heat transfer coefficients show fair to good agreement with predictions of prior and popular correlations. But superior predictions in both trend and magnitude are achieved with the annular flow model.

© 2014 Elsevier Ltd. All rights reserved.

1. Introduction

For many decades, condensation has been implemented in power generation, chemical, pharmaceutical, and refrigeration and air conditioning applications. The high heat transfer coefficients associated with condensation have also made possible the development of thermal management solutions for a number of modern technologies that demand the transfer or dissipation of large amounts of heat from small volumes. These include cooling systems for high power density electronic and power devices. These cooling systems generally rely on boiling to acquire the heat from the device, and reject the heat to the ambient by condensation [1]. Much of the research on these systems has been focused on the heat acquisition by boiling, including pool boiling [2–4], channel flow boiling [5–7], jet [8–11] and spray [12–15], as well as enhanced surfaces [16–18] and hybrid cooling configurations [19]. Condensation, however, has received far less emphasis, and

most of the design tools for condenser design are adopted directly from tools developed decades ago for more conventional power generation and refrigeration and air conditioning applications.

Several well-defined flow regimes have been identified for condensation inside horizontal tubes which, in order of decreasing quality, include pure vapor, annular, slug, bubbly and pure liquid [20]. Both flow regime maps and regime transition relations have been recommended to determine dominant flow regimes [21–26]. The annular regime has attracted the most attention because of its prevalence over a large fraction of the tube length and ability to deliver high heat transfer coefficients. The annular regime consists of a thin film that sheathes the inner walls of the condensation tube, shear driven by a faster moving central vapor core.

While vapor shear is the main driving force in annular condensation, gravity can also play an important role for condensation inside horizontal tubes, which is manifest in stratification of liquid toward the bottom of the inner surface. This results in a relatively thick liquid film towards the bottom, compared to a very thin film or no film at the top. Conditions that yield pronounced stratification effects are generally associated with a strong influence of gravity on the magnitude and spatial variations of the condensation heat transfer coefficient.

* Corresponding author. Tel.: +1 (765) 494 5705; fax: +1 (765) 494 0539.

E-mail address: mudawar@ecn.purdue.edu (I. Mudawar).

URL: <https://engineering.purdue.edu/BTFL> (I. Mudawar).

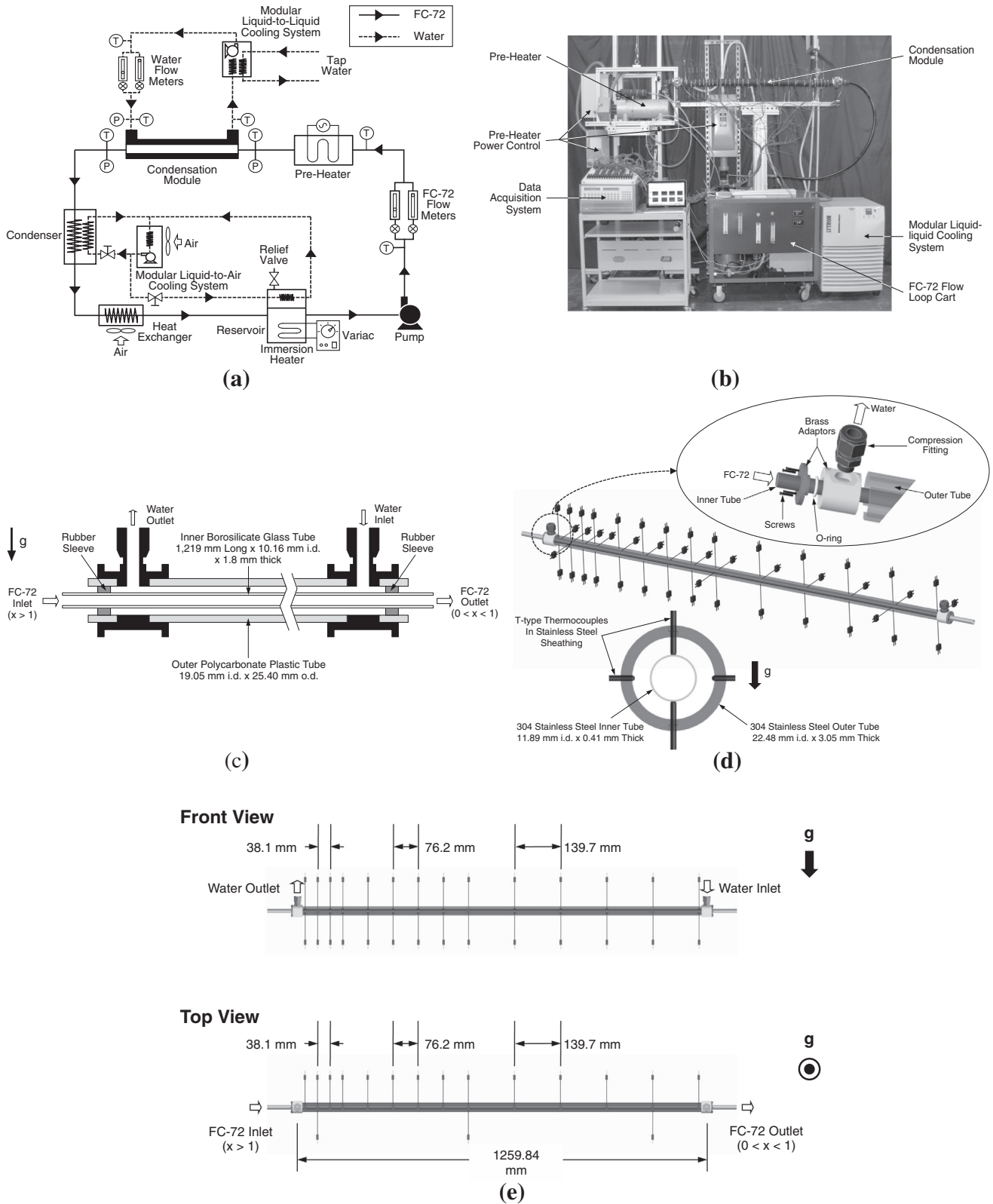


Fig. 1. (a) Schematic diagram of condensation facility. (b) Photo of facility. (c) Construction of flow visualization module. (d) Construction of heat transfer module. (e) Location of thermocouples for temperature measurements of outer wall of inner tube and cooling water in heat transfer module.

is achieved by transferring heat from the FC-72 to the first water loop via a condensation test module. A separate condenser is used to transfer heat to the second water cooling loop. A perfluorinated

fluid made by 3M-company, FC-72 is a colorless and odorless dielectric fluid developed mostly for electronics cooling applications. **Table 1** provides representative thermophysical properties

Table 1
Thermophysical properties of saturated FC-72, Water and R134a at 65 °C.

	k_f [W/m K]	μ_f [kg/m s]	$c_{p,f}$ [J/kg K]	σ [mN/m]	h_{fg} [kJ/kg]	ρ_f [kg/m ³]	ρ_g [kg/m ³]
FC-72	0.0529	396×10^{-6}	1120	7.47	92	1569	17.35
Water	0.6454	433×10^{-6}	4184	65.36	2345	981	0.161
R134a	0.0618	115×10^{-6}	1723	3.16	132	1026	100.50

of this fluid along with those of other commonly used working fluids (water and R134a) at a saturation temperature of 65 °C corresponding to the average operating pressure for the present study of 1.34 bar.

The primary FC-72 loop contains a sealed reservoir from which the liquid is circulated with the aid of a gear pump. The liquid is passed through one of several rotameters for flow rate measurement following which it is converted to slightly superheated vapor by a 14.2 kW Watlow pre-heater. The FC-72 vapor is then routed into the condensation module, where it is partially returned to liquid state by rejecting heat to a counter-flow of water from the first water loop. The FC-72 two-phase mixture exiting the condensation module is cooled further by rejecting heat to the second water cooling loop via a plate-type condenser. Prior to returning to the reservoir, any residual FC-72 vapor is converted to subcooled liquid by an air-cooled condenser. The FC-72 temperature is measured at the pre-heater's inlet, and the temperature and pressure at both the inlet and outlet of the condensation module. The water temperature is measured at the inlet and outlet of the condensation module. The FC-72 temperature and pressure are also measured at several locations in the primary loop.

The first water cooling loop absorbs the heat from the FC-72 in the condensation module and rejects it to tap water using a 14-kW modular Lytron cooling system consisting of a reservoir, pump and liquid-to-liquid heat exchanger. The second water cooling loop consists of a 1.46-kW modular Lytron system containing a reservoir, pump and water-to-air heat exchanger.

Before performing any condensation tests, the FC-72 is carefully deaerated in the primary loop's reservoir using immersion heaters and a condensation coil that is cooled by the second water cooling loop. Full deaeration requires simultaneous vigorous boiling and condensation of the FC-72 for 30 min, during which any non-condensable gases are purged to the ambient.

2.2. Condensation module for flow visualization

Two separate condensation modules are used in this study, one for flow visualization and the other for heat transfer measurements. These modules possess similar dimensions but feature different construction materials.

The flow visualization module features transparent tube-in-tube construction. As shown in Fig. 1(c), the FC-72 flows horizontally through the inner tube, and the water flows in the opposite direction through the annulus between the inner and outer tubes. The inner 1219-mm long tube is made from borosilicate glass and has a 10.16-mm i.d. and wall thickness of 1.8 mm. The outer tube is made from polycarbonate plastic (Lexan), which, like the inner tube, features high transparency but a much lower thermal conductivity, and has a 19.05-mm i.d. and 25.4-mm o.d. The inlet and outlet of the condensation module are fitted with rubber sealing sleeves between the inner the outer tubes, which result in a condensation length of 1143 mm for flow visualization. The FC-72 inlet and outlet of the flow visualization module are fitted with type-T thermocouples and pressure transducers. Both the inlet and outlet of the waterside are fitted with type-T thermocouples.

Flow visualization is achieved with a high-speed Photron Fastcam video camera fitted with a Nikon 105-mm magnification lens.

The camera is positioned normal to the front of the condensation module, which is back lit by an array of 15 high power white 5-W LEDs.

2.3. Condensation module for heat transfer measurements

The second module is used exclusively for obtaining detailed heat transfer measurements. This module has an overall design very similar to that of the flow visualization module except for the use of different materials to facilitate accurate heat transfer measurements. Fig. 1(d) illustrates the construction of the inner and outer tubes of the heat transfer module, which features a condensation length of 1259.8 mm. Both tubes are made from 304 stainless steel. The inner tube has an 11.89-mm i.d. and wall thickness of 0.41 mm, and the outer tube 22.48-mm i.d. and 3.05-mm wall thickness. A compromise between the need to minimize resistance to radial heat conduction between the FC-72 and water, versus that to minimize axial wall conduction effects is achieved with a combination of small thickness of the inner tube and relatively low thermal conductivity of stainless steel. A thick outer layer of fiberglass insulation that is applied over the entire condensation module minimizes any heat loss to the ambient.

Like the flow visualization module, the heat transfer module contains temperature and pressure instrumentation at the inlets and outlets for both fluids. However, the heat transfer module features 45 type-T thermocouples, 28 of which are installed in 14 diametrically opposite pairs on the outer top and bottom surfaces of the inner tube to capture any gravity induced temperature differences. Layout of these thermocouples is illustrated in the front view of the heat transfer module in Fig. 1(e). The thermocouple pairs are closer to one another in the FC-72 inlet region to capture the sharp axial variations in wall temperature near the inlet. 14 other thermocouples are inserted into the water annulus at the same axial locations as the wall thermocouples as illustrated in the top view in Fig. 1(e). Three additional thermocouples are inserted in the water diametrically opposite to three of the 14 main water thermocouples to capture any asymmetry in the water temperatures. All thermocouples are made from 0.21-mm diameter thermocouple wire with a bead diameter of 0.79 mm.

2.4. Operating conditions and measurement uncertainty

Two separate series of experiments are performed using the two condensation modules. The experiments using the flow visualization module are focused on both identifying the condensation flow regimes and capturing the interfacial behavior of the condensing film. The second series of experiments are performed with the heat transfer module to capture the detailed spatial variations of the condensation heat transfer coefficient. In both series of experiments, the thermodynamic equilibrium quality of FC-72 at the inlet is maintained slightly above unity.

The flow visualization experiments consist of 110 sets of operating conditions. As indicated in Table 2, they include 22 FC-72 mass velocities in the range of $G_{FC} = 26.65\text{--}343.79$ kg/m² s and a broad range of water mass velocities of $G_w = 12.22\text{--}476.64$ kg/m² s. Also included in Table 2 are values of FC-72 inlet quality, $x_{e,in}$, inlet temperature, $T_{FC,in}$, inlet pressure, $P_{FC,in}$, outlet quality,

Table 2
Experimental operating conditions for the flow visualization tests.

	FC-72					Cooling water			q_w [W]	$x_{e,out}$	$Re_{f,out}$
	$x_{e,in}$	\dot{m}_{FC} [g/s]	G_{FC} [kg/m ² s]	$T_{FC,in}$ [°C]	$P_{FC,in}$ [kPa]	\dot{m}_w [g/s]	G_w [kg/m ² s]	ΔT_w [°C]			
Max.	1.12	27.89	343.79	73.38	147.37	64.97	476.64	26.14	836.35	0.80	2508.22
Min.	1.03	2.16	26.65	64.79	105.50	1.67	12.22	3.01	182.12	0.05	534.52

Table 3
Experimental operating conditions for the condensation heat transfer tests.

	FC-72						Cooling water			q_w [W]	$x_{e,out}$	$Re_{f,out}$
	$x_{e,in}$	\dot{m}_{FC} [g/s]	G_{FC} [kg/m ² s]	$T_{FC,in}$ [°C]	$\Delta T_{FC,sat,TP}$ [°C]	$P_{FC,in}$ [kPa]	\dot{m}_w [g/s]	G_w [kg/m ² s]	ΔT_w [°C]			
Max.	1.07	64.02	576.83	83.7	3.16	200.61	83.31	308.32	10.07	3145.7	0.55	7926.79
Min.	1.02	4.32	38.96	61.43	0.05	103.44	66.64	246.66	1.97	686.42	0.01	876.61

$x_{e,out}$, and outlet film Reynolds number, $Re_{f,out}$, as well as the amount of heat transferred from FC-72 to the cooling water, q_w . Of the 110 tests, 104 resulted in saturated two-phase mixture conditions at the exit, while 6 tests ($G_{FC} = 26.65$ kg/m² s with $G_w = 18.33, 24.44, 30.55,$ and 36.66 kg/m² s and $G_{FC} = 39.94$ kg/m² s with $G_w = 45.83$ and 54.99 kg/m² s) produced subcooled liquid exit conditions. Table 2 excludes the values of $x_{e,out}$ and $Re_{f,out}$ for those 6 tests.

The heat transfer experiments consist of 45 sets of operating conditions. As indicated in Table 3, these tests include 15 FC-72 mass velocities in the range of $G_{FC} = 38.96$ – 576.83 kg/m² s with $G_w = 246.66, 277.48$ and 308.32 kg/m² s for each FC-72 mass velocity. To preclude uncertainties from cooling water entrance effects, heat transfer data are measured only within the FC-72 upstream condensation length of $z = 0$ – 807.7 mm. Inlet FC-72 quality values in the range of $x_{e,in} = 1.025$ – 1.074 produce upstream single-phase superheated vapor regions 8.08– 74.31 -mm long (1.0–9.2% of the 807.7 mm length considered in the heat transfer measurements). Of the 45 tests, 39 resulted in two-phase mixture conditions at the exit with $x_{e,out} = 0.01$ – 0.55 and $Re_{f,out} = 876.61$ – 7926.79 , respectively. The remaining 6 tests ($G_{FC} = 38.97$ kg/m² s with $G_w = 246.66, 277.48$ and 308.32 kg/m² s, and $G_{FC} = 77.91$ kg/m² s with $G_w = 246.66, 277.48$ and 308.32 kg/m² s) resulted in subcooled liquid conditions at the exit with two-phase condensation lengths in the range of 274.62– 557.33 mm (34–69% of the 807.7-mm measurement length). Table 3 excludes the values of $x_{e,out}$ and $Re_{f,out}$ for these 6 tests.

The pressure transducers used throughout the condensation facility possess a measurement uncertainty of $\pm 0.5\%$, and uncertainties of the thermocouples are smaller than ± 0.4 °C. Uncertainties in the outer diameter and wall thickness of the condensing tube used for heat transfer measurements are ± 0.08 and ± 0.03 mm, respectively. The uncertainties of the outer diameter and wall thickness of the outer tube of the same condensation module are ± 0.13 and ± 0.18 mm, respectively. Combining these uncertainties with those associated with determination of fluid properties yields overall uncertainties in determining heat transfer rate, vapor quality, and condensation heat transfer coefficient of 10.01%, 11.23% and 11.41%, respectively.

3. Flow visualization results

3.1. Condensation regimes

It is crucial to point out that, because the FC-72 film covers the inner wall of the inner tube, the captured video images represent two separate interfaces overlaid on one another. Nonetheless, the

video method used and construction of the flow visualization module could clearly identify all dominant flow regimes.

One key objective of the present flow visualization experiments is to complement earlier experiments by the authors [39], which utilized a different construction for the flow visualization module. In the prior experiments, the flow paths for the FC-72 and water are reversed compared to the present flow visualization module. The water flow was passed through a 304 stainless steel tube and the FC-72 in the opposite direction through an annulus between the 5.99-mm o.d. stainless steel tube and an 12.2-mm wide square outer channel made from polycarbonate plastic; the hydraulic diameter for the FC-72 flow was 7.12 mm. A key advantage of the present flow visualization module is its simple circular geometry for the FC-72 flow, which is the same geometry adopted for the heat transfer measurements.

To map condensation regimes, video images are captured for 110 sets of operating conditions at three 381-mm long inlet, middle and outlet regions centered at $z = 190, 571$ and 952 mm, respectively, from the FC-72 inlet. These tests yield *superheated vapor* flow in the inlet region, while, as indicated earlier, 6 tests produce *subcooled liquid* flow in the outlet region. After careful examination of the video images, four dominant flow regimes are identified: *stratified*, *stratified-wavy*, *wavy-annular with gravity influence*, and *wavy-annular without gravity influence*. When computing parameters for assessment of flow regime maps using the data reduction technique discussed later, the temperatures of both the FC-72 and cooling water are assumed to vary linearly along the condensation length of the flow visualization module. The FC-72 parameters used in the flow regime maps include mass velocity, G_{FC} , thermodynamic equilibrium quality, x_e , superficial liquid velocity, j_f , modified superficial vapor velocity, j_g^* , modified Weber number, We^* , Lockhart–Martinelli parameter, X_{tt} , and dimensionless superficial vapor velocity, j_g^* .

Fig. 2 shows representative sequential images of the FC-72 condensation film along the inner wall of the glass tube for the aforementioned four condensation regimes. The duration of each sequence is 0.3 s, with individual images separated by 0.0125 s. The images presented in Fig. 2(a) are captured in the middle region, centered at $z = 571$ mm from the FC-72 inlet, and Fig. 2(b–d) in the exit region, centered at $z = 952$ mm. It is noted that all high-speed video clips are captured at 8000 frame/s with a resolution of 512×256 pixels.

Fig. 2(a) shows representative images of the *stratified* regime corresponding to $G_{FC} = 26.65$ kg/m² s, $x_e = 0.43$ and $G_w = 36.66$ kg/m² s. Computed values for the FC-72 flow parameters in this figure are $j_f = 0.01$, $j_g^* = 3.00$, $We^* = 5.52$, $X_{tt} = 0.17$ and $j_g^* = 0.25$. The *stratified* regime is characterized by complete separation between liquid and vapor, which occurs at low mass velocities for both phases. Weak vapor and liquid inertia at these conditions enable

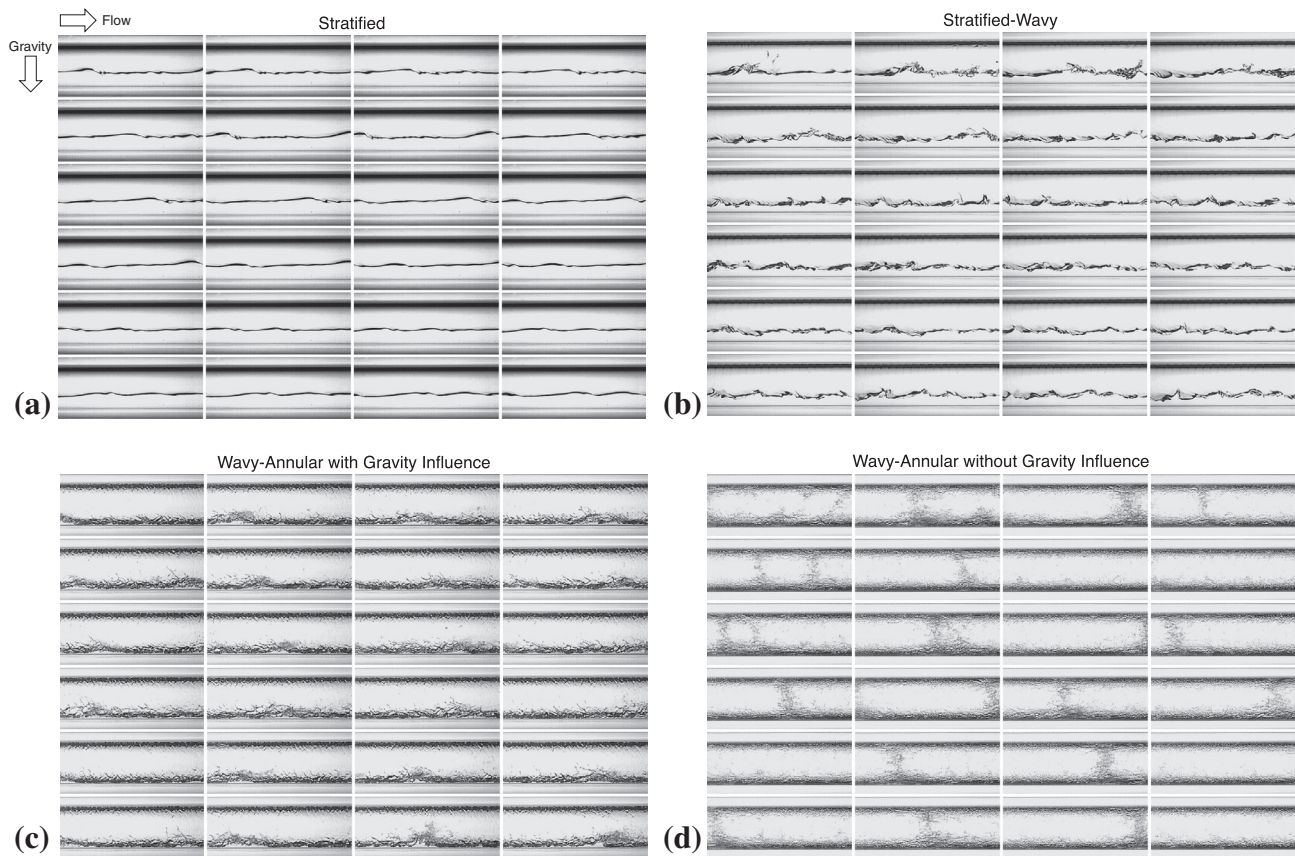


Fig. 2. Sequential images of (a) *stratified* regime with $G_{FC} = 26.65 \text{ kg/m}^2 \text{ s}$, $x_e = 0.43$ and $G_w = 36.66 \text{ kg/m}^2 \text{ s}$, (b) *stratified-wavy* regime with $G_{FC} = 53.25 \text{ kg/m}^2 \text{ s}$, $x_e = 0.29$ and $G_w = 61.10 \text{ kg/m}^2 \text{ s}$, (c) *wavy-annular with gravity influence* regime with $G_{FC} = 132.94 \text{ kg/m}^2 \text{ s}$, $x_e = 0.65$ and $G_w = 183.32 \text{ kg/m}^2 \text{ s}$, and (d) *wavy-annular without gravity influence* regime with $G_{FC} = 265.19 \text{ kg/m}^2 \text{ s}$, $x_e = 0.76$ and $G_w = 366.66 \text{ kg/m}^2 \text{ s}$. Total duration of each sequence is 0.3 s, with individual images separated by 0.0125 s.

gravity to play a dominant role, accumulating the liquid at the bottom of the tube and vapor above. The liquid–vapor interface appears to be laminar, which can be explained by the weak vapor shear corresponding to low G_{FC} . Relatively large waves are observed at the interface at times, but these waves quickly subside into the liquid layer.

Representative images of the *stratified-wavy* regime are depicted in Fig. 2(b) corresponding to $G_{FC} = 53.25 \text{ kg/m}^2 \text{ s}$, $x_e = 0.29$ and $G_w = 61.10 \text{ kg/m}^2 \text{ s}$. Computed values for this test are $j_f = 0.02$, $j'_g = 3.83$, $We^* = 6.58$, $X_{tt} = 0.32$ and $j_g^* = 0.32$. Increasing G_{FC} from the previous *stratified* regime increases velocity difference between the vapor and liquid as well as the vapor shear stress; both intensify interfacial instability. There is also an increase in the amplitude of the interfacial waves, but this amplitude is still too small to ensure any appreciable liquid contact with the top of the tube. The liquid in the *stratified-wavy* regime is still accumulated on the bottom in the form of a thick liquid layer, which demonstrates the important influence of gravity for this regime. Fig. 2(b) shows liquid droplets are broken off the wave crests and entrained into the vapor flow.

As the mass velocity of FC-72 is increased further, the vapor shear becomes strong enough to spread the liquid along the entire tube perimeter. This behavior is captured in Fig. 2(c) corresponding to $G_{FC} = 132.94 \text{ kg/m}^2 \text{ s}$, $x_e = 0.65$ and $G_w = 183.32 \text{ kg/m}^2 \text{ s}$, and computed FC-72 parameters of $j_f = 0.03$, $j'_g = 21.37$, $We^* = 20.06$, $X_{tt} = 0.08$ and $j_g^* = 1.76$. This flow regime is identified as *wavy-annular with gravity influence*. The effect of gravity is manifest by the thicker film at the bottom compared to a much thinner film at the top. There is also increased turbulence and interfacial instability, with the film's interface at the bottom incurring chaotic large

waves, while the film at the top exhibits mostly small capillary ripples. Droplets are created mostly from breakup of waves on the bottom liquid layer.

A large increase in G_{FC} greatly increases the vapor velocity and therefore interfacial shear, which dwarfs the influence of gravity altogether. This results in the *wavy-annular without gravity influence* regime depicted in Fig. 2(d) for $G_{FC} = 265.19 \text{ kg/m}^2 \text{ s}$, $x_e = 0.76$ and $G_w = 366.66 \text{ kg/m}^2 \text{ s}$, and corresponding computed FC-72 parameters of $j_f = 0.04$, $j'_g = 49.61$, $We^* = 37.17$, $X_{tt} = 0.05$ and $j_g^* = 4.08$. Here, the liquid film is spread uniformly along the inner perimeter. The film's motion is dictated by the large vapor shear, which is also responsible for formation of both large waves and small ripples. High shear also causes breakup of minute liquid droplets from the wave crests; these droplets are entrained in the form of clusters that are entrained in the vapor core.

3.2. Flow regime maps

The experimental flow regime data are compared to four different types of previously published regime maps. Table 4 provides information concerning working fluid, hydraulic diameter, and quality range of the original maps. Fig. 3(a) shows a comparison between the present flow regime data and prior G versus x_e regime maps [20,29]. Despite differences in hydraulic diameter and channel geometry between the present study and the original map, this map shows fair ability in capturing the present annular regime data. Notice that a combination of high G_{FC} and high x_e produces annular flow (designated in the original map as wavy-annular and smooth-annular regimes), which also includes the present *wavy-annular with gravity influence* and *wavy-annular without grav-*

Table 4
Details of prior flow regime maps.

	Mandhane et al. [21]	Breber et al. [22]	Soliman [23,24]	Wang et al. [29]	Chen et al. [25]	Kim and Mudawar [26]
Working fluid	Air–water	R11, R113, R12, n-pentane, steam	Steam, R113, R12	R134a	R134a	FC-72
D_h [mm]	12.7–165.1	4.8–50.8	7.4–12.7	1.46	12, 14	1
Quality range	–	–	0.2–0.95	0.03–0.94 (inlet quality)	–	0–1

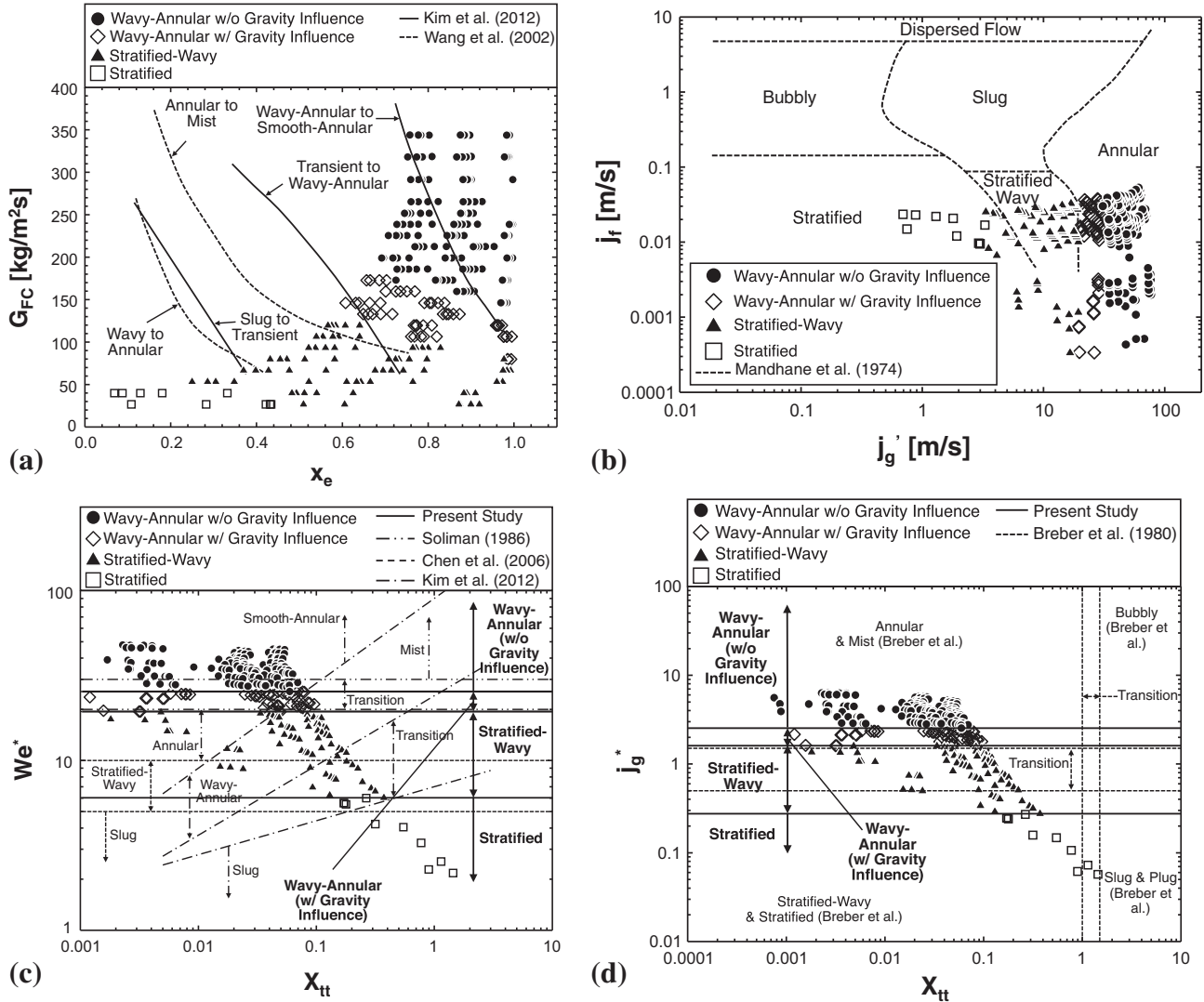


Fig. 3. Comparison of present flow regime data with flow regime maps of: (a) Wang et al. [29] and Kim et al. [20], (b) Mandhane et al. [21], (c) Soliman [24], Chen et al. [25] and Kim et al. [26], and (d) Breber et al. [22].

ity influence regimes. For small G_{FC} and small x_e values, gravity plays a dominant role in the present study, which is reflected in the stratified-wavy and stratified regimes.

Fig. 3(b) compares the present flow regime data with the regime map of Mandhane et al. [21], which is based on superficial liquid and vapor velocities, j_f and j_g , respectively. The map shown here is modified by replacing j_g by j_g^* ($= \sqrt{\rho_g/\rho_{air}} j_g$), as recommended by Dobson and Chato [36] to extend Mandhane et al.'s original air–water map to several types of refrigerants. Using the modified superficial vapor velocity, Fig. 3(b) shows that this map predicts the present four flow regime data with fair accuracy. Notice the far stronger dependence of flow regimes on the modified superficial vapor velocity than the superficial liquid velocity.

The experimental flow regime data are compared to two other types of maps that compensate for differences in working fluid and tube geometry with the aid of appropriate dimensionless

groups. Fig. 3(c) compares the present data with those of Soliman [24], Chen et al. [25] and Kim and Mudawar [26]. Soliman derived flow regime boundary relations by balancing destructive and stabilizing forces using the modified Weber number, We^* , and the Lockhart–Martinelli parameter, X_{tt} , where

$$We^* = 2.45 Re_g^{0.64} \left(\frac{\mu_g^2}{\rho_g \sigma D} \right)^{0.3} / \phi_g^{0.4} \quad \text{for } Re_f \leq 1250, \quad (1a)$$

and

$$We^* = 0.85 Re_g^{0.79} \left(\frac{\mu_g^2}{\rho_g \sigma D} \right)^{0.3} \left[\left(\frac{\mu_g}{\mu_f} \right)^2 \left(\frac{\rho_f}{\rho_g} \right) \right]^{0.084} \left(\frac{X_{tt}}{\phi_g^{2.55}} \right)^{0.157} \quad \text{for } Re_f > 1250, \quad (1b)$$

where

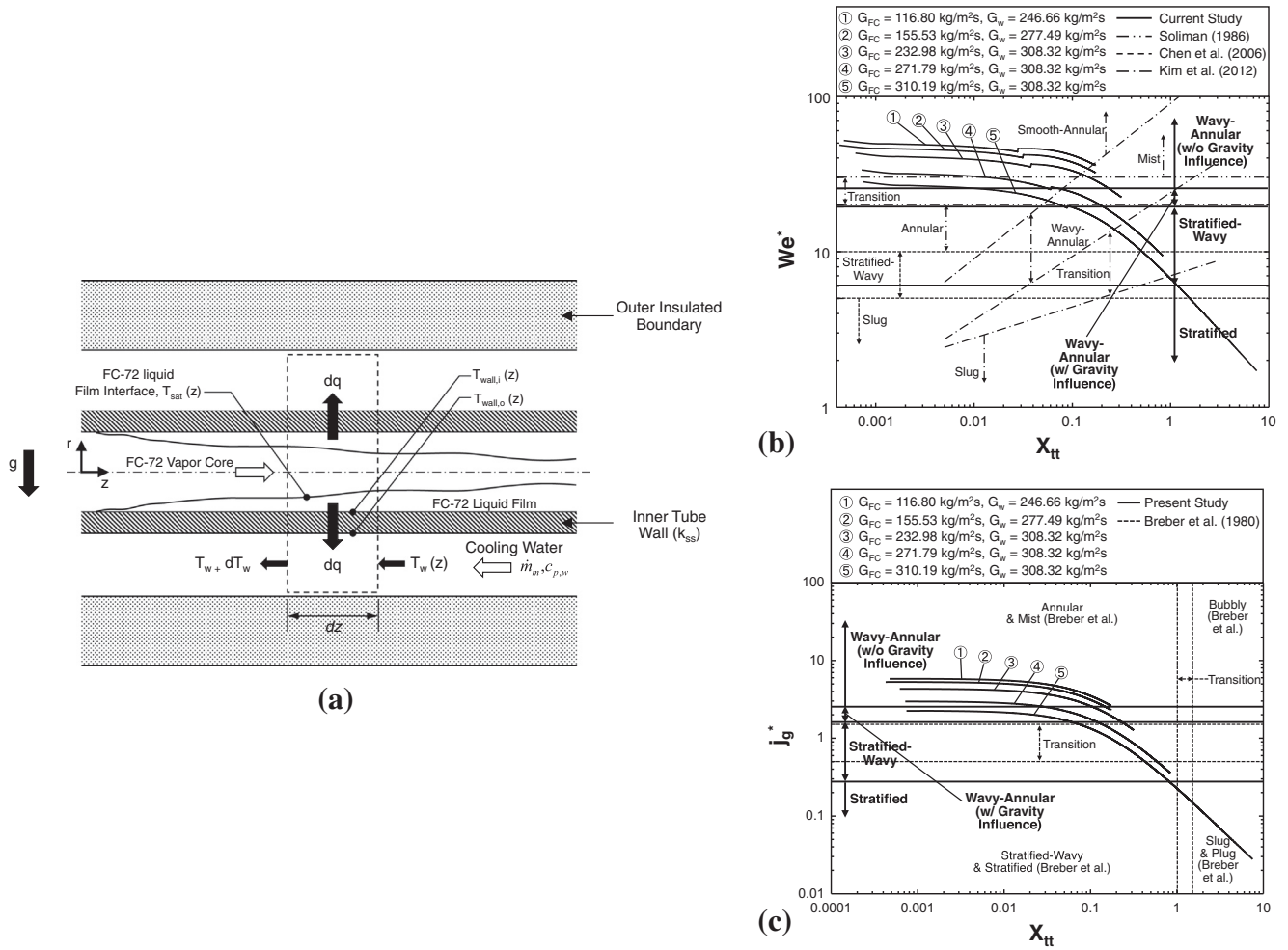


Fig. 4. (a) Thermal model used to determine the local condensation heat transfer coefficient for FC-72. (b) Operating conditions for heat transfer module superimposed on prior flow regime maps based on We^* versus X_{tt} , along with predictions of Soliman [24], Chen et al. [25] and Kim et al. [20]. (c) Operating conditions for heat transfer module superimposed on prior flow regime map based on J_g^* versus X_{tt} , along with predictions of Breber et al. [22].

$$Re_g = x_e G D / \mu_g, \tag{2a}$$

$$Re_f = G(1 - x_e) D / \mu_f, \tag{2b}$$

$$X_{tt} = \left(\frac{1 - x_e}{x_e} \right)^{0.9} \left(\frac{\rho_g}{\rho_f} \right)^{0.5} \left(\frac{\mu_f}{\mu_g} \right)^{0.1} \tag{3}$$

and

$$\phi_g = 1 + 1.09 X_{tt}^{0.039}. \tag{4}$$

Using Soliman’s dimensionless groups, Chen et al. [25] recommended relations for the boundaries between his annular and stratified-wavy regimes and between stratified-wavy and plug regimes based on experimental data for horizontal condensation of R134a inside 12 and 14-mm microfin tubes. Also using Soliman’s dimensionless groups, Kim and Mudawar [26] recently proposed the following boundary relations for condensation of FC-72:

$$\text{Smooth – annular to wavy – annular : } We^* = 90 X_{tt}^{0.5}, \tag{5a}$$

$$\text{Wavy – annular to transition : } We^* = 24 X_{tt}^{0.41}, \tag{5b}$$

$$\text{Transition to slug : } We^* = 7 X_{tt}^{0.2}. \tag{5c}$$

It should be emphasized that We^* in the above relations and all We^* relations hereafter are defined according to Eqs. (1a) and (1b) depending on the magnitude of Re_f . Fig. 3(c) shows fair agreement between the present flow regime data and the predictions of the $We^* - X_{tt}$ map. However, the present regime data are better segregated with the aid of the following regime boundary relations based on modified Weber number:

$$\text{Stratified : } We^* < 6.03, \tag{6a}$$

$$\text{Stratified to wavy stratified : } 6.03 \leq We^* < 19.39, \tag{6b}$$

$$\text{Wavy stratified to wavy-annular with gravity influence : } 19.39 \leq We^* < 25.46, \tag{6c}$$

$$\text{Wavy-annular without gravity influence : } We^* \geq 25.46. \tag{6d}$$

Fig. 3(d) compares the present flow regime data to a fourth type of regime map proposed by Breber et al. [22], which utilizes the coordinates of dimensionless superficial vapor velocity, J_g^* , and X_{tt} , where

$$J_g^* = \frac{x_e G}{\sqrt{g D \rho_g (\rho_f - \rho_g)}}. \tag{7}$$

Breber et al. proposed annular flow is achieved for $J_g^* > 1.5$ and $X_{tt} < 1.0$, and stratified and stratified-wavy flow for $J_g^* < 0.5$ and $X_{tt} < 1.0$. Again, this map predicts the present flow regimes fairly

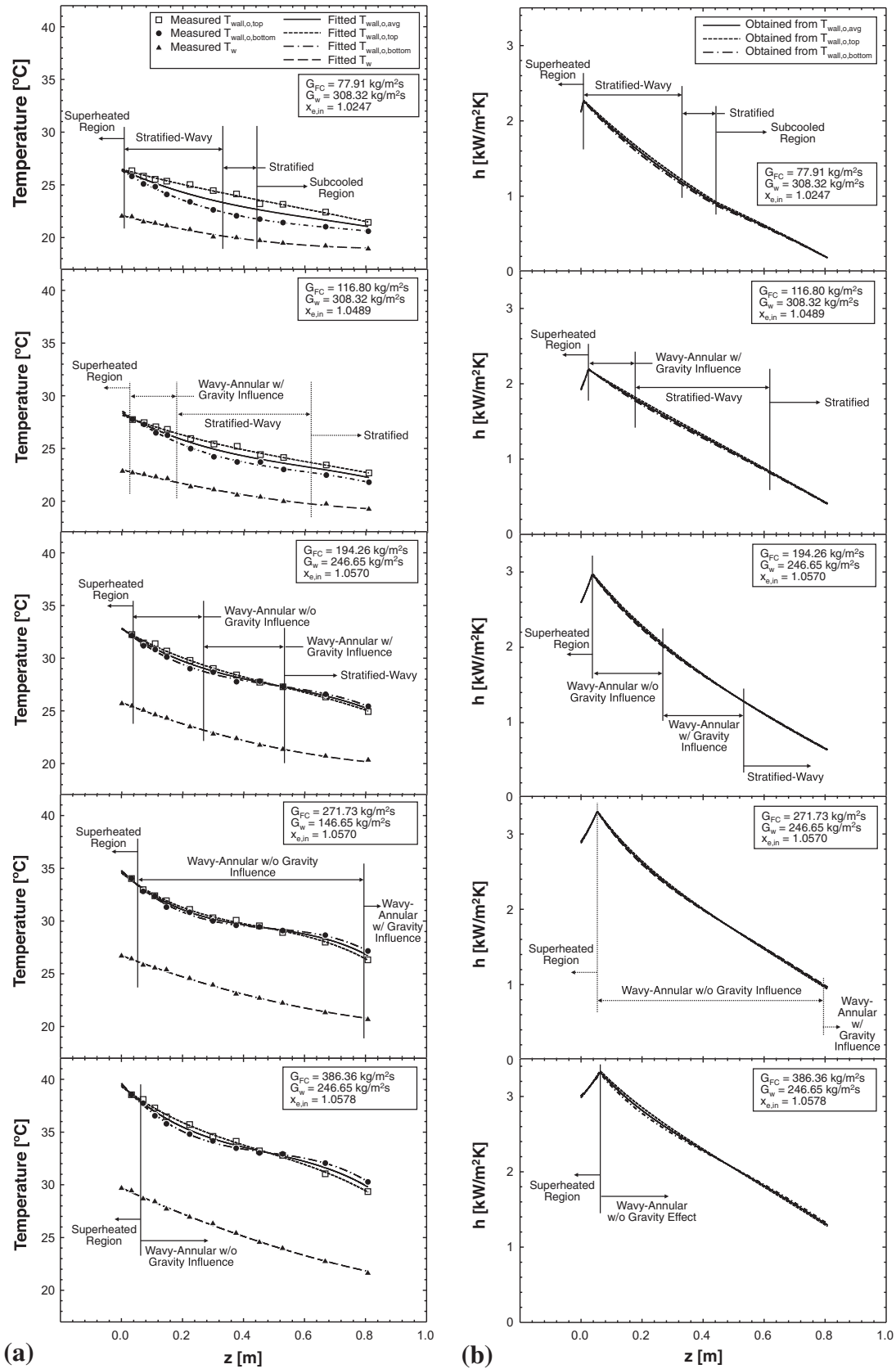


Fig. 5. Axial variations of (a) outer wall temperatures (top, bottom and average) of condensation tube and cooling water temperature in heat transfer module, and (b) corresponding condensation heat transfer coefficients for five combinations of FC-72 and water mass velocities.

well, however, the present regime data are better segregated according to the following boundary relations based on dimensionless superficial vapor velocity:

$$\text{Stratified: } j_g^* < 0.28, \quad (8a)$$

$$\text{Stratified to wavy stratified: } 0.28 \leq j_g^* < 1.61, \quad (8b)$$

$$\text{Wavy stratified to wavy-annular with gravity influence: } 1.61 \leq j_g^* < 2.54, \quad (8c)$$

$$\text{Wavy-annular without gravity influence: } j_g^* \geq 2.54. \quad (8d)$$

Overall, the four types of regime maps show fair ability in predicting the present flow regimes, especially in terms of overall regime trends. However, these maps are not able to predict conditions where the influence of gravity can be negated. This limitation is corrected with the aid of the new regime boundary relations, Eqs. (6a)–(6d) and (8a)–(8d). Nonetheless, the reader is reminded about the fundamental weakness of all regime maps, which stems from the inability to accurately describe boundaries between drastically different flow regimes that are characterized by different dimensionless groups using a single two-dimensional plot.

4. Heat transfer results

4.1. Data reduction technique

As discussed in [33], the local condensation heat transfer coefficient in the heat transfer condensation module is determined with the aid of thermal model that is illustrated in Fig. 4(a). Condensation along the liquid film's interface is assumed to occur at saturation temperature, $T_{sat}(z)$. Because pressure drop across the condensation length is quite small, the saturation pressure, $P_{sat}(z)$, used to determine $T_{sat}(z)$ is calculated from a linear curve fit between the measured inlet pressure, P_{in} , and outlet pressure, P_{out} .

The water temperature, $T_w(z)$, and outer wall temperature of the inner tube, $T_{wall,o}(z)$, are determined from curve fits to their respective measured values. A differential amount of heat, dq , that is transferred from the FC-72 to the water is equal to the differential rise in sensible energy of the water. For the portion of the condensation length where $x_e < 1$, the local condensation heat transfer coefficient, $h(z)$, of FC-72 is determined from

$$dq = (\pi D_i dz) h (T_{sat} - T_{wall,i}) = \frac{T_{wall,i} - T_{wall,o}}{\frac{\ln(D_o/D_i)}{2\pi k_{ss} dz}} = \dot{m}_w c_{p,w} dT_w. \quad (9)$$

For the short upstream superheated region before the liquid film begins to develop, the temperature of the FC-72 vapor, $T_g(z)$, is determined from the heat balance $\dot{m}_{FC} c_{p,g} dT_g = \dot{m}_w c_{p,w} dT_w$, and x_e from $x_e = 1 + c_{p,g}(T_g - T_{sat})/h_{fg}$, which is also used to determine the location z where $x_e = 1$. The heat transfer coefficient for the superheated region is obtained by replacing T_{sat} in Eq. (9) with the local temperature of the superheated vapor.

$$dq = (\pi D_i dz) h (T_g - T_{wall,i}) = \frac{T_{wall,i} - T_{wall,o}}{\frac{\ln(D_o/D_i)}{2\pi k_{ss} dz}} = \dot{m}_w c_{p,w} dT_w. \quad (10)$$

For the saturated region ($x_e < 1$), the local flow rate of the condensing film, $\dot{m}_f(z)$, is obtained by integrating the relation $d\dot{m}_f = dq/h_{fg}$ from the location where $x_e = 1$. The local thermodynamic equilibrium quality in the same region is given by $x_e = (\dot{m}_{FC} - \dot{m}_f)/\dot{m}_{FC}$.

4.2. Determination of local flow regimes

Unlike the flow visualization module used to assess the condensation flow regimes as discussed in the previous section and

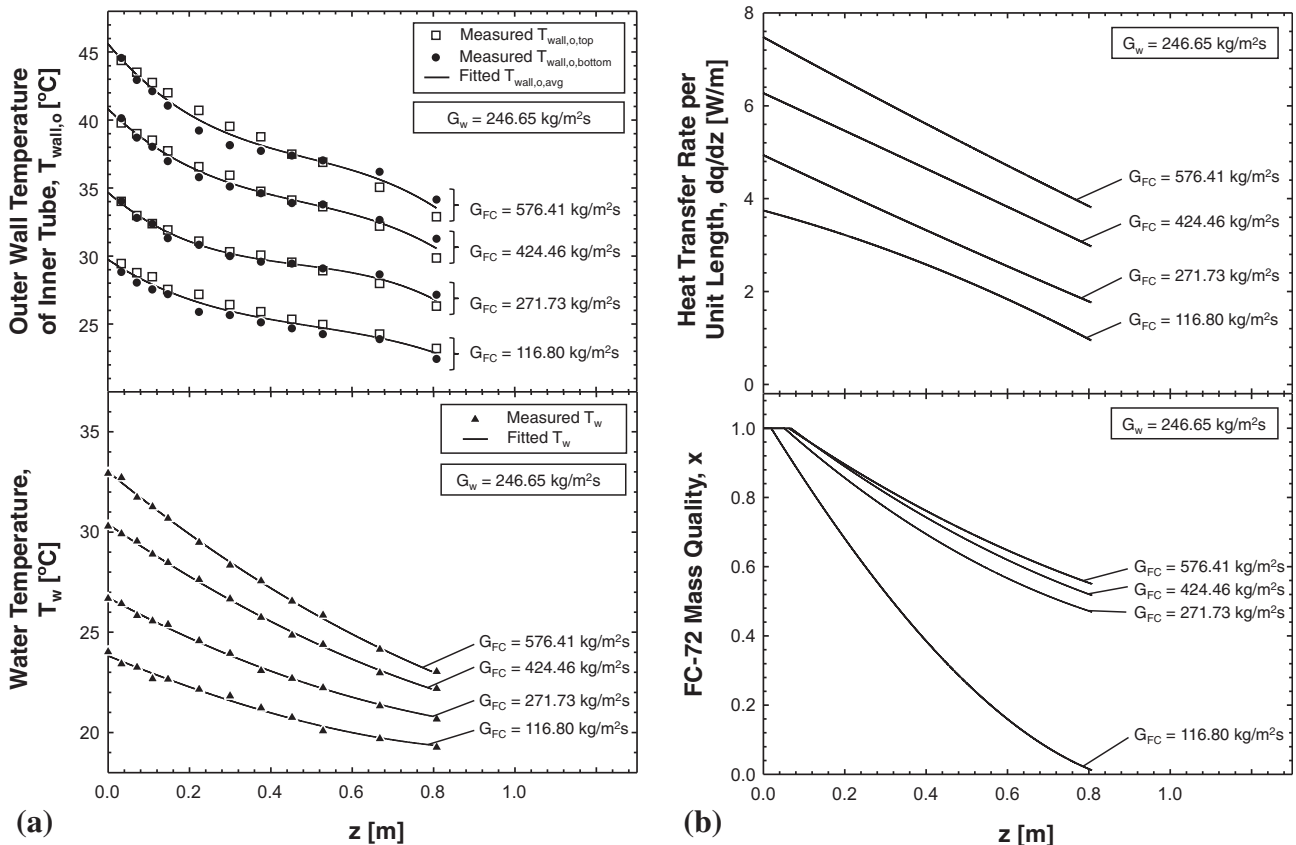


Fig. 6. Axial variations of (a) measured and fitted temperatures of outer wall of condensation tube and cooling water in heat transfer module, and (b) heat transferred from FC-72 to cooling water per unit distance and quality of FC-72 for four FC-72 mass velocities.

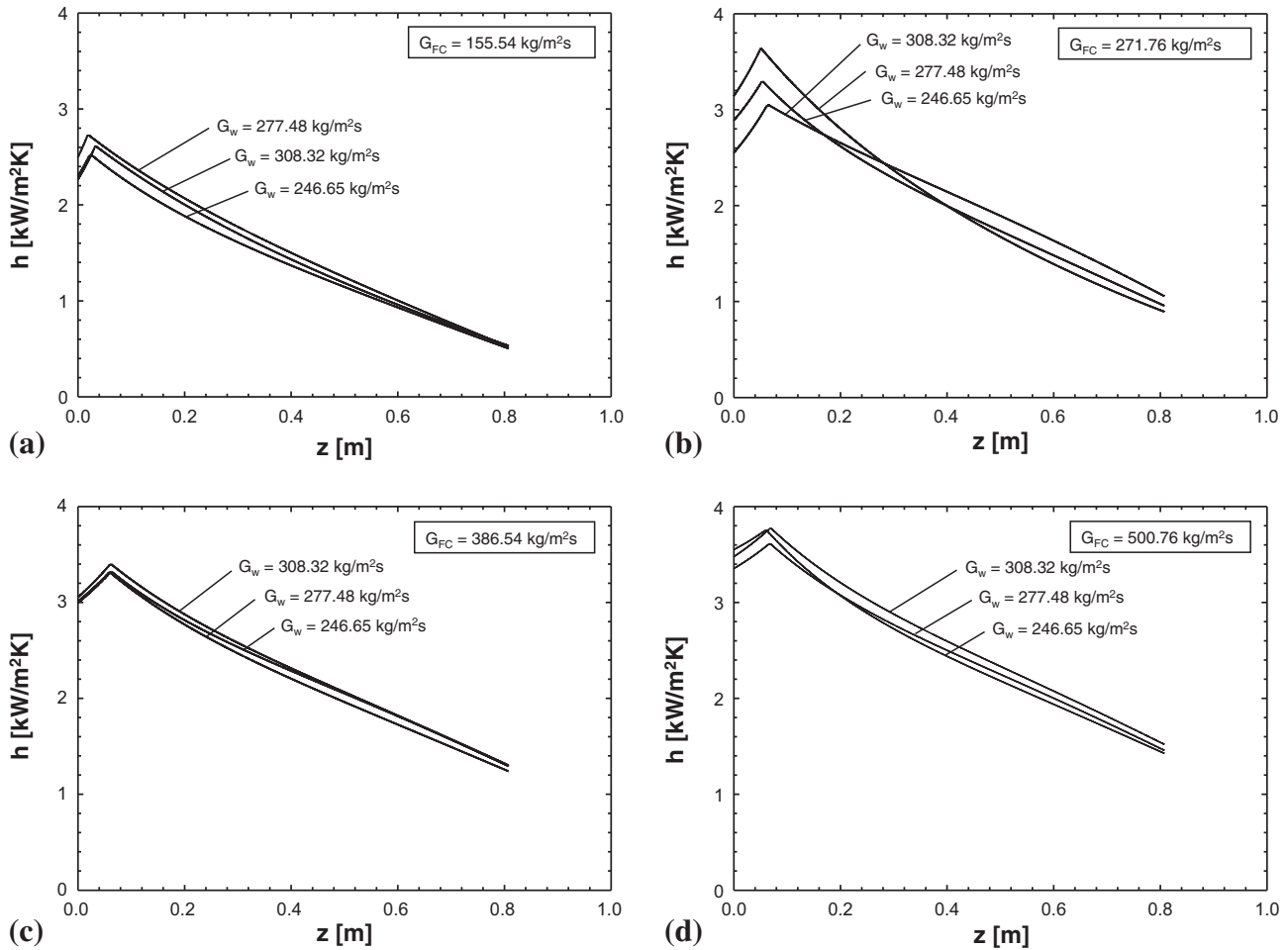


Fig. 7. Axial variation of experimentally determined condensation heat transfer coefficient in heat transfer module for different water mass velocities and FC-72 mass velocities of (a) $G_{FC} = 155.54 \text{ kg/m}^2 \text{ s}$, (b) $G_{FC} = 271.76 \text{ kg/m}^2 \text{ s}$, (c) $G_{FC} = 386.54 \text{ kg/m}^2 \text{ s}$, and (d) $G_{FC} = 500.76 \text{ kg/m}^2 \text{ s}$.

Fig. 3(a–d), the heat transfer module used to measure $h(z)$ does not allow video access to the condensing flow. Therefore, the flow regime transition relations discussed in the previous section are used to relate the measured heat transfer coefficient data to well-defined flow regimes. Fig. 4(b) and (c) shows five different combinations of G_{FC} and G_w from the heat transfer module test matrix presented in $We^* - X_{tt}$ and $J_g^* - X_{tt}$ maps, respectively, excluding the short upstream superheated region. Indicated are the new regime boundary relations given by Eqs. (6a)–(6d) in Fig. 4(b) and Eqs. (8a)–(8d) in Fig. 4(c). Both sets of regime boundary relations provide consistent predictions of the local flow regimes with only minor discrepancies. For the heat transfer study, the flow regime boundary relations based on dimensionless superficial vapor velocity, J_g^* , are utilized to determine the local flow regimes for the heat transfer results presented hereafter.

4.3. Circumferential variations of heat transfer parameters

Fig. 5(a) shows, for five sets of operating conditions, axial variations of wall temperatures of the condensation tube measured by the thermocouples on the top and bottom of the outer tube wall, $T_{wall,o,top}$ and $T_{wall,o,bottom}$, respectively, and the measured cooling water temperature, T_w . Also shown are third-order polynomial curve fits to axial distance for the top outer wall temperature, bottom outer wall temperature, average of the top and bottom outer wall temperatures, and water temperature. These plots show rela-

tively short single-phase superheated vapor regions for all five cases; temperature differences between the top outer wall and the bottom outer wall are miniscule in the inlet region. For the lowest FC-72 mass velocity at $G_{FC} = 77.91 \text{ kg/m}^2 \text{ s}$, subcooled liquid flow occupies nearly half of the condensation length in the downstream region. After the short superheated region, the *stratified-wavy* and *stratified* regimes are encountered in sequence in the upstream region. Notice that the subcooled liquid region is absent for all other higher G_{FC} . With increasing G_{FC} , the condensation length occupied by the *stratified* and *stratified-wavy* regimes becomes shorter, displaced upstream by the *wavy-annular with gravity influence* and *wavy-annular without gravity influence* regimes in order. Notice that most of the condensation length is occupied by the *wavy-annular without gravity influence* regime for the two larger FC-72 mass velocities of $G_{FC} = 271.73$ and $386.36 \text{ kg/m}^2 \text{ s}$. Fig. 5(a) also shows the differences between the top and bottom outer wall temperatures are more significant in the *stratified-wavy* and *stratified* regimes, caused by accumulation of liquid and better cooling towards the bottom of the tube. The maximum differences between the top and bottom outer wall temperatures in the *stratified-wavy* and *stratified* regimes are 2.65 and 2.62 °C, respectively. In the *wavy-annular without gravity influence* and *wavy-annular with gravity influence* regimes, the temperature difference is less significant (especially for the former regime) as the liquid film is now spread circumferentially around the inner perimeter in response to increasing vapor shear. The maximum

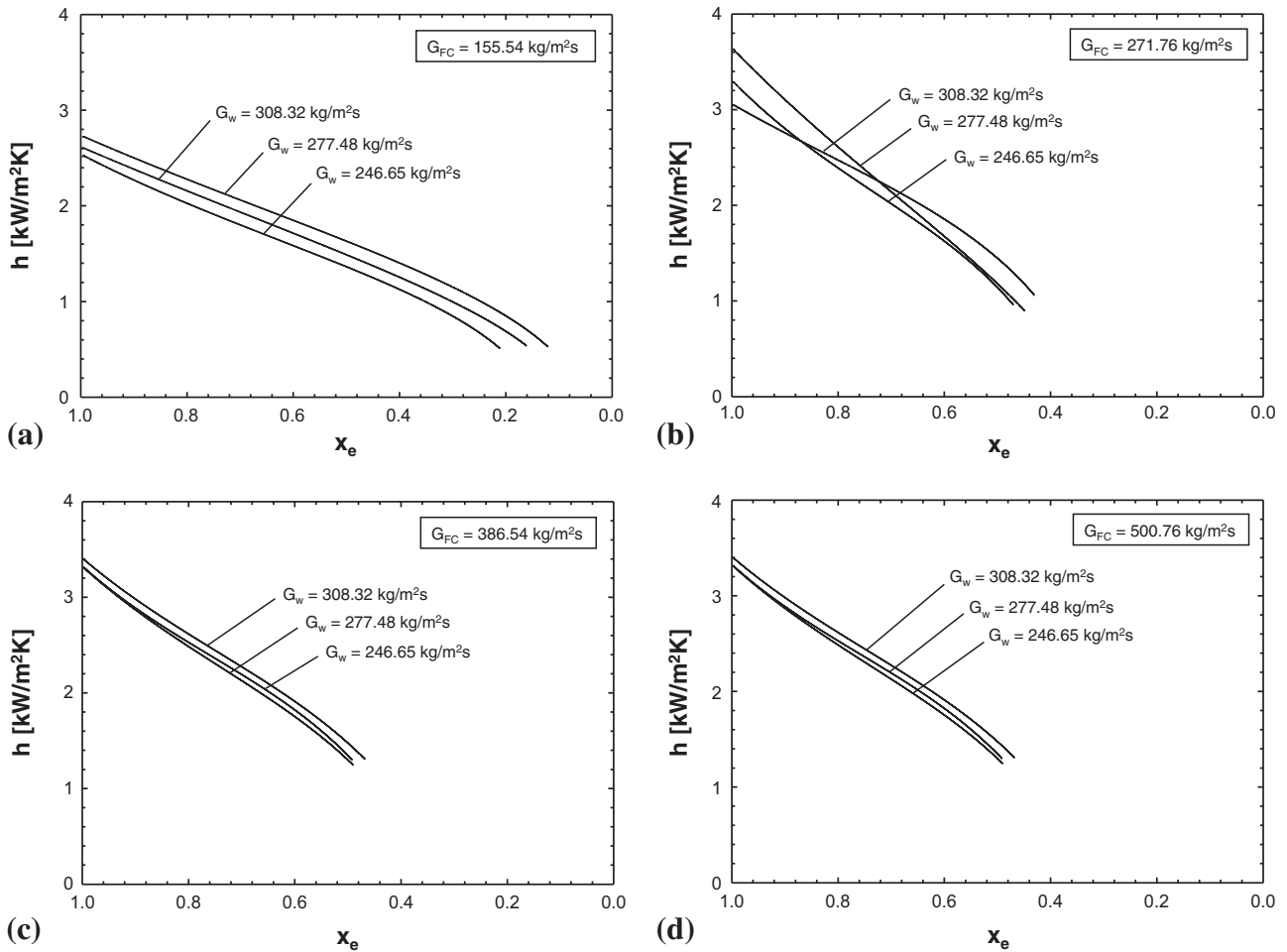


Fig. 8. Variation of experimentally determined local condensation heat transfer coefficient in heat transfer module with thermodynamic equilibrium quality for different water mass velocities and FC-72 mass velocities of (a) $G_{FC} = 155.54 \text{ kg/m}^2 \text{ s}$, (b) $G_{FC} = 271.76 \text{ kg/m}^2 \text{ s}$, (c) $G_{FC} = 386.54 \text{ kg/m}^2 \text{ s}$, and (d) $G_{FC} = 500.76 \text{ kg/m}^2 \text{ s}$. These plots exclude the superheated region data captured in Fig. 7 from the inlet to the peak point.

differences between the top and bottom outer wall temperatures in the *wavy-annular without gravity influence* and *wavy-annular with gravity influence* regimes are 1.68 and 1.00 °C, respectively.

Fig. 5(b) shows axial variations of the condensation heat transfer coefficient obtained using the top outer wall temperature, bottom outer wall temperature, and average temperature of the two for the same operating conditions as those in Fig. 5(a). Like the temperature measurements, differences among the condensation heat transfer coefficients obtained from the three different outer wall temperatures are more significant in the *stratified-wavy* and *stratified* regimes. The maximum differences between the condensation heat transfer coefficients obtained from the top and bottom outer wall temperatures in the *stratified-wavy* and *stratified* regimes are 7.77% and 7.60%, respectively. The maximum differences between the condensation heat transfer coefficients obtained from the top and bottom outer wall temperatures in the *wavy-annular without gravity influence* and *wavy-annular with gravity influence* regimes are 4.66% and 3.15%, respectively. It is important to note that all heat transfer results presented hereafter are based on the average outer wall temperature.

4.4. Heat transfer trends

Fig. 6(a) shows axial variations of the outer wall temperature of the inner tube, $T_{wall,o}$, and the water temperature, $T_w(z)$, for four different combinations of FC-72 and water mass velocities; both

variations are determined from third-order polynomial curve fits to axial distance. These distributions are then used to calculate corresponding variations depicted in Fig. 6(b) for the amount of heat transferred from the FC-72 to the water per unit length, dq/dz , using Eqs. (9) and (10), and the FC-72 mass quality, x , using $x = (\dot{m}_{FC} - \dot{m}_f) / \dot{m}_{FC}$. Fig. 6(b) shows dq/dz for all FC-72 mass velocities is highest in the upstream region, where the condensate film is thinnest, and decreases gradually towards the outlet because of increasing film thickness. Additionally, dq/dz increases with increasing G_{FC} because of increased vapor shear. As expected, Fig. 6(b) shows x is highest in the upstream region and decreases gradually towards the outlet.

Fig. 7(a–d) shows axial variations of the experimentally determined local FC-72 heat transfer coefficient, h , in both the single-phase superheated vapor region and film condensation regions for $G_{FC} = 155.54\text{--}500.76 \text{ kg/m}^2 \text{ s}$ and $G_w = 246.65\text{--}308.32 \text{ kg/m}^2 \text{ s}$. For most cases, the heat transfer coefficient increases rather sharply in the superheated vapor region near the inlet, reaching peak value where the annular liquid film is initiated. Note that a clearly defined single-phase vapor flow region upstream of the peak point would yield a fairly constant h value. The unexpected trend of increasing h in the upstream region may be explained by the film formation commencing in a circumferentially nonuniform manner within the predominantly single-phase vapor region where $x_e > 1$. The peak value is believed to occur where the film initiation becomes complete. As shown in Fig. 7(a–d), h decreases

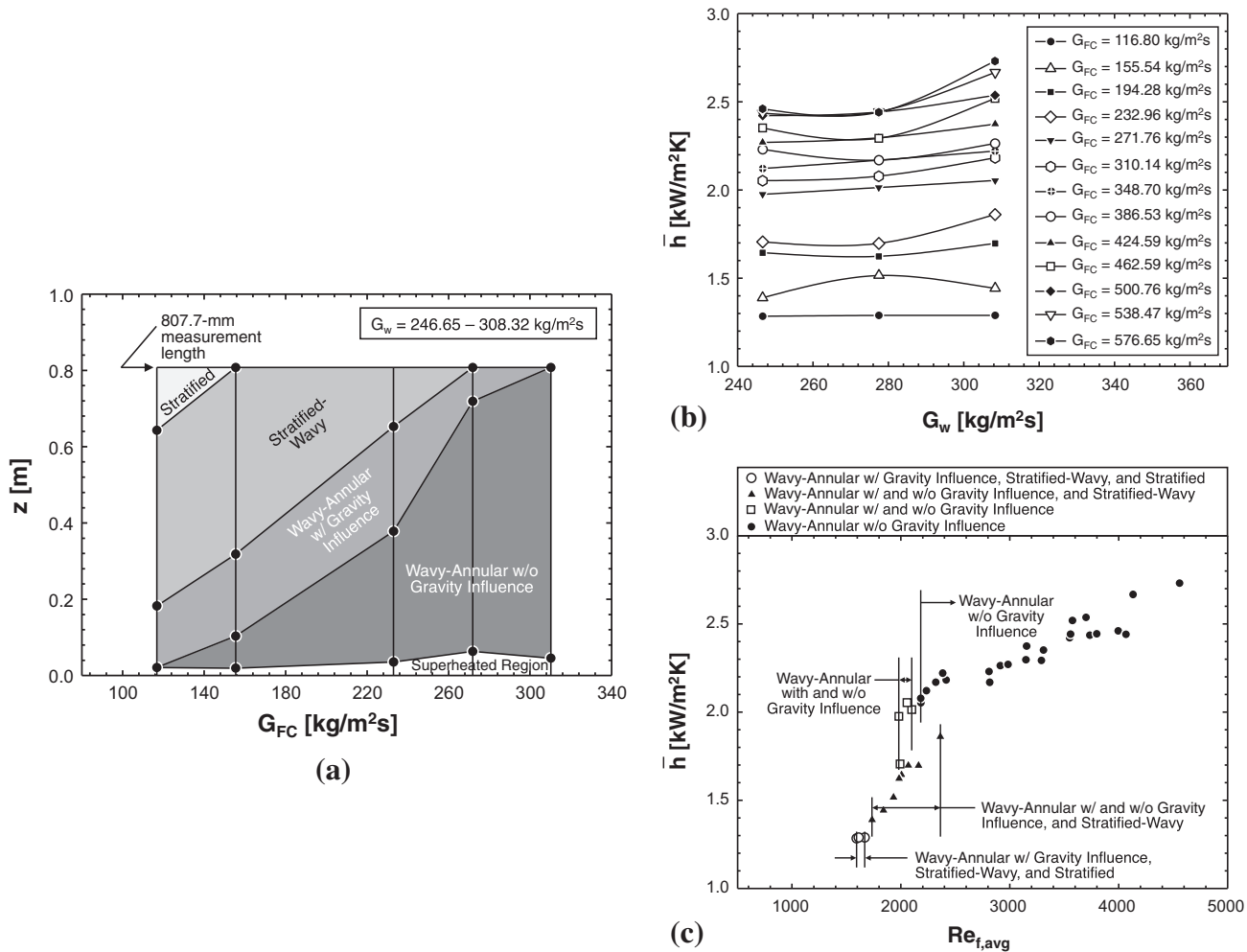


Fig. 9. (a) Variations of flow regimes along condensation length for different FC-72 mass velocities. (b) Variation of experimentally-determined average condensation heat transfer coefficient with water mass velocity for different FC-72 mass velocities. (c) Variation of experimentally-determined average condensation heat transfer coefficient with film Reynolds number averaged over two-phase region.

downstream of the peak value for all FC-72 mass velocities because of the increasing liquid film thickness. Comparing Fig. 7(a–d) shows h increases with increasing G_{FC} , which can be attributed to thinning of the film by the increasing vapor shear.

Fig. 8(a–d), which exclude the region from the inlet to the peak point captured in Fig. 7(a–d), shows a monotonic decrease in h with x_e for four FC-72 mass velocities. This trend is attributed to the aforementioned axial increase in film thickness.

4.5. Axial span of flow regimes

Fig. 9(a) shows axial spans of the four flow regimes over the 807.7-mm measurement length for five FC-72 mass velocities of $G_{FC} = 116.80, 155.53, 232.98, 271.79$ and 310.19 kg/m² s and $G_w = 246.65$ – 308.32 kg/m² s. For each value of G_{FC} , there is a relatively short upstream superheated region. The stratified regime is present only over a short downstream distance for the lowest mass velocity of $G_{FC} = 116.80$ kg/m² s, and absent for the higher FC-72 mass velocities. The stratified-wavy regime is present for the three lowest FC-72 mass velocities, and the axial span of the same regime decreases with increasing G_{FC} ; the stratified-wavy regime is non-existent at $G_{FC} = 271.79$ kg/m² s. The wavy-annular with gravity influence regime is present for a broad range of G_{FC} from 116.80 to 271.79 kg/m² s, but the axial span of this regime is relatively short for all four cases. The wavy-annular without gravity

influence regime is present from $G_{FC} = 155.53$ kg/m² s, and its axial span increases with increasing G_{FC} . Notice that only the wavy-annular without gravity influence regime is present over the entire two-phase region after the short superheated region for the higher FC-72 mass velocity of $G_{FC} = 310.19$ kg/m² s.

4.6. Average condensation heat transfer coefficient

Fig. 9(b) shows the variation of the average condensation heat transfer coefficient, \bar{h} , with mass velocity of the cooling water, G_w , for different FC-72 mass velocities. The values presented in Fig. 9(b) are averaged over the two-phase condensation region, thus excluding the upstream superheated vapor region. \bar{h} increases with increasing G_{FC} because of the increased interfacial shear and thinning of the liquid film. Fig. 9(c) shows \bar{h} increases monotonically with the film Reynolds number, $Re_{f,avg}$, averaged over the two-phase condensation region.

5. Condensation model and correlations

5.1. Formulation of annular flow model

Recently, Park et al. [33] developed a control volume model for annular flow corresponding to condensation in downflow. The model was based on the assumptions of a smooth interface

Table 5
Annular flow model relations [33].

<p>Mass conservation</p> $\frac{d\dot{m}_l}{dz} - \Gamma_{fg} = 0; \quad \frac{d\dot{m}_g}{dz} + \Gamma_{fg} = 0; \quad \dot{m}_f = \rho_f \int_0^\delta u_f \pi (D - 2y) dy; \quad \dot{m}_g = \rho_g \bar{u}_g \pi (D - 2\delta)^2 / 4; \quad \Gamma_{fg} = q_w'' \pi D / h_{fg}$
<p>Momentum conservation for liquid film</p> $\tau = \mu_f \left(1 + \frac{\epsilon_m}{\nu_f}\right) \frac{du_f}{dy} = \left(-\frac{dp}{dz}\right) \frac{A_{f,s}}{P_{f,y}} + \frac{\tau_i P_{f,\delta} + \Gamma_{fg} u_i}{P_{f,y}} \quad A_{f,s} = \frac{\pi}{4} (D - 2y)^2 - \frac{\pi}{4} (D - 2\delta)^2, \quad P_{f,y} = \pi (D - 2y), \quad P_{f,\delta} = \pi (D - 2\delta)$
<p>Velocity profile across the film</p> $u_f(y) = \frac{\delta}{\mu_f} \left(-\frac{dp}{dz}\right) \int_0^{y/\delta} \frac{A_{f,s}}{P_{f,y}} \left(1 + \frac{\epsilon_m}{\nu_f}\right)^{-1} d\left(\frac{y}{\delta}\right) + \frac{\delta}{\mu_f} (\tau_i P_{f,\delta} + \Gamma_{fg} u_i) \int_0^{y/\delta} \frac{1}{P_{f,y}} \left(1 + \frac{\epsilon_m}{\nu_f}\right)^{-1} d\left(\frac{y}{\delta}\right); \quad u_i = u_f(\delta)$
<p>Pressure gradient</p> $-\frac{dp}{dz} = \frac{\frac{\mu_f \dot{m}_f}{\rho_f \delta^2} (\tau_i P_{f,\delta} + \Gamma_{fg} u_i) \int_0^1 \left[\frac{P_{f,y}}{P_{f,y}} \int_0^{y/\delta} \frac{1}{P_{f,y}} \left(1 + \frac{\epsilon_m}{\nu_f}\right)^{-1} d\left(\frac{y}{\delta}\right) \right] d\left(\frac{y}{\delta}\right)}{\int_0^1 \left[\frac{P_{f,y}}{P_{f,y}} \int_0^{y/\delta} \frac{1}{P_{f,y}} \left(1 + \frac{\epsilon_m}{\nu_f}\right)^{-1} d\left(\frac{y}{\delta}\right) \right] d\left(\frac{y}{\delta}\right)}$
<p>Momentum conservation for vapor core</p> $\tau_i = \frac{1}{P_{f,\delta}} \left[A_g \left(-\frac{dp}{dz}\right) - \frac{d(\rho_g u_g^2 A_g)}{dz} - \Gamma_{fg} u_i \right]; \quad A_g = \pi (D - 2\delta)^2 / 4$
<p>Interfacial shear stress relation [42,43]</p> $\tau_i = \frac{1}{2} f_i \rho_g (\bar{u}_g - u_i)^2 + \frac{(\bar{u}_g - u_i) \Gamma_{fg}}{2 P_{f,\delta}}$ <p>$f_i = 16/Re_c$ for $Re_c < 2000$; $f_i = 0.079 Re_c^{-0.25}$ for $2000 \leq Re_c < 20,000$, $f_i = 0.046 Re_c^{-0.2}$ for $Re_c \geq 20,000$; $Re_c = \rho_g (\bar{u}_g - u_i) (D - 2\delta) / \mu_g$</p>
<p>Eddy momentum diffusivity [44]</p> $\frac{\epsilon_m}{\nu_f} = -\frac{1}{2} + \frac{1}{2} \sqrt{1 + 4K^2 y^{+2} \left[1 - \exp\left(-\sqrt{1 - \frac{y^+}{\delta^+}} \frac{y^+}{A^+}\right)\right]^2 \left(1 - \frac{y^+}{\delta^+}\right) \frac{\tau_i}{\tau_w}}; \quad K = 0.4; \quad A^+ = 26 \left(1 + 30.18 \mu_f \rho_f^{0.5} \tau_w^{-1.5} \frac{dp}{dz}\right)^{-1}$
<p>Turbulent Prandtl number [45]</p> $Pr_T = 1.4 \exp\left(-15 \frac{y^+}{\delta^+}\right) + 0.66; \quad \delta^+ = \delta u^* / \nu_f$
<p>Heat transfer coefficient</p> $h = \frac{q_w''}{T_{sat} - T_w} = \frac{\rho_f c_{p,f} u^*}{T_s} = \frac{\rho_f c_{p,f} u^*}{\int_0^{\delta^+} \frac{q_w''}{\rho_f c_{p,f}} \left(\frac{1}{Pr_T} + \frac{1}{Pr_T^*}\right)^{-1} dy^*} = \frac{\rho_f c_{p,f} u^*}{\int_0^{\delta^+} \left(\frac{\rho}{\rho^*}\right) \left(\frac{1}{Pr_T} + \frac{1}{Pr_T^*}\right)^{-1} dy^*}$

between the annular liquid film and vapor core, and circumferential symmetry of the liquid film. This model is briefly summarized below with all key equations provided in Table 5.

Fig. 10(a) and (b) shows control volumes encompassing a portion of the liquid film and the entire vapor core, respectively. The mass flow rates of the liquid and vapor are \dot{m}_f and \dot{m}_g , respectively, and Γ_{fg} represents the rate of interfacial mass transfer due to condensation per unit distance. The annular flow model involves application of mass and momentum conservation to the differential liquid and vapor control volumes. Neglecting axial momentum changes in the liquid film, momentum conservation for the liquid is used to develop relations for shear stress, τ , across the film, liquid velocity, $u_f(y)$, and axial pressure gradient, $-dp/dz$. Next, applying momentum conservation to the vapor control volume provides a relation for the interfacial shear stress, τ_i , in terms of the pressure gradient. The interfacial shear stress is proportional to the product of interfacial friction factor, f_i [42], and square of velocity difference between the vapor core and interface, plus interfacial momentum transfer [43]. The heat flux across the liquid film is related to the liquid temperature gradient according to $q''/q_w'' = (Pr_f^{-1} + Pr_T^{-1} \epsilon_m/\nu_f) dT^+/dy^+$,

where $T^+ = \rho_f c_{p,f} u^* (T - T_w) / q_w''$, $y^+ = y u^* / \nu_f$, $u^* = \sqrt{\tau_w / \rho_f}$, and Pr_T is the turbulent Prandtl number (ϵ_m/ϵ_h). The model uses an expression for Pr_T derived by Mudawar and El-Masri [45] based on experimental data by Ueda et al. [46]. Mudawar and El-Masri also developed a turbulent mixing length profile based on an eddy-diffusivity profile measured by Ueda et al. This profile was modified by Kim and Mudawar [44] to obtain a relation for eddy momentum diffusivity in a shear-driven film that accounts for axial pressure gradient per [47,48]. This relation is used in the annular flow model to determine the local condensation heat transfer coefficient using the relations provided in Table 5.

5.2. Model predictions

Fig. 10(c–f) shows the model predictions of the variations of film Reynolds number, Re_f , vapor core's Reynolds number, Re_g , interfacial shear stress, τ_i , and film thickness, δ , respectively, with thermodynamic equilibrium quality for four sets of operating conditions. Fig. 10(c) shows Re_f increases monotonically with decreasing x_e (i.e., increasing z). The fastest increase in Re_f is associated with the largest G_{FC} , which results in the highest interfacial shear and heat transfer coefficient. On the other hand, Fig. 10(d) shows Re_g decreasing with decreasing x_e , again with the fastest decrease associated with the highest G_{FC} . Fig. 10(e) shows τ_i decreasing with decreasing x_e , with the largest G_{FC} yielding the largest τ_i and steepest decrease. Fig. 10(f) shows δ increases along the axial condensation length as more vapor is condensed into liquid. Notice that a relatively small film thickness is maintained along the entire condensation length for the three larger values of G_{FC} because of high interfacial shear.

5.3. Predictions of local condensation heat transfer coefficient

Fig. 11(a–d) shows, for four FC-72 mass velocities, the variations of the experimentally-determined local condensation heat transfer coefficient, h , with thermodynamic equilibrium quality, x_e , along with predictions of the annular model and six popular and recent correlations. The heat transfer coefficient results and predictions are associated with the two-phase region only and utilizing the average outer wall temperature. The correlations used are summarized in Table 6. The experimentally-determined heat transfer coefficient is highest near $x_e = 1$ and decreases monotonically with decreasing x_e because of the afore-mentioned axial thickening of the condensation film. This trend is captured by the annular model

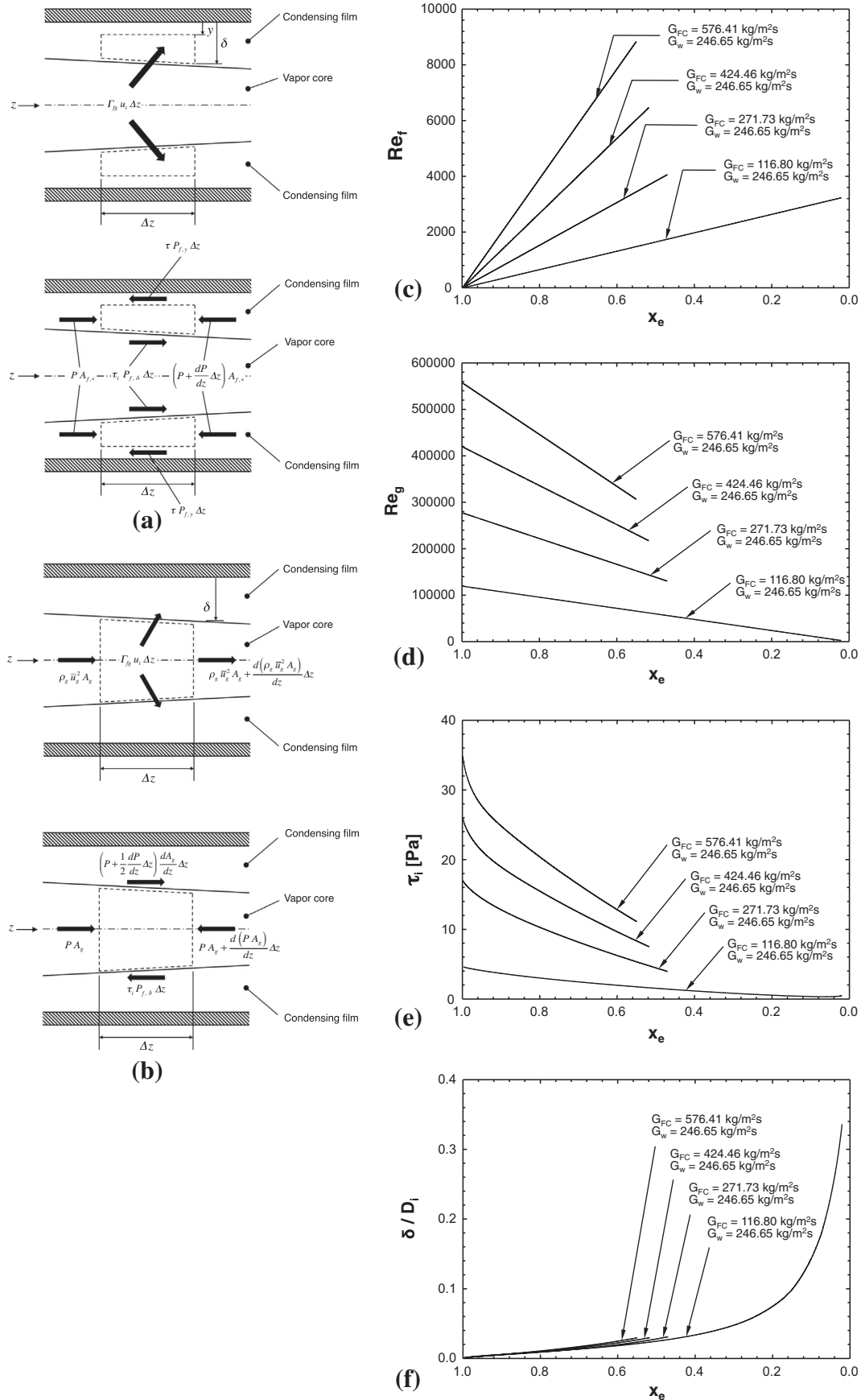


Fig. 10. Momentum and force components for (a) liquid film control volume and (b) vapor core control volume. Predicted variations of (c) liquid film Reynolds number, (d) vapor core Reynolds number, (e) interfacial shear stress, and (f) liquid film thickness with equilibrium quality for different combinations of FC-72 and water mass velocities.

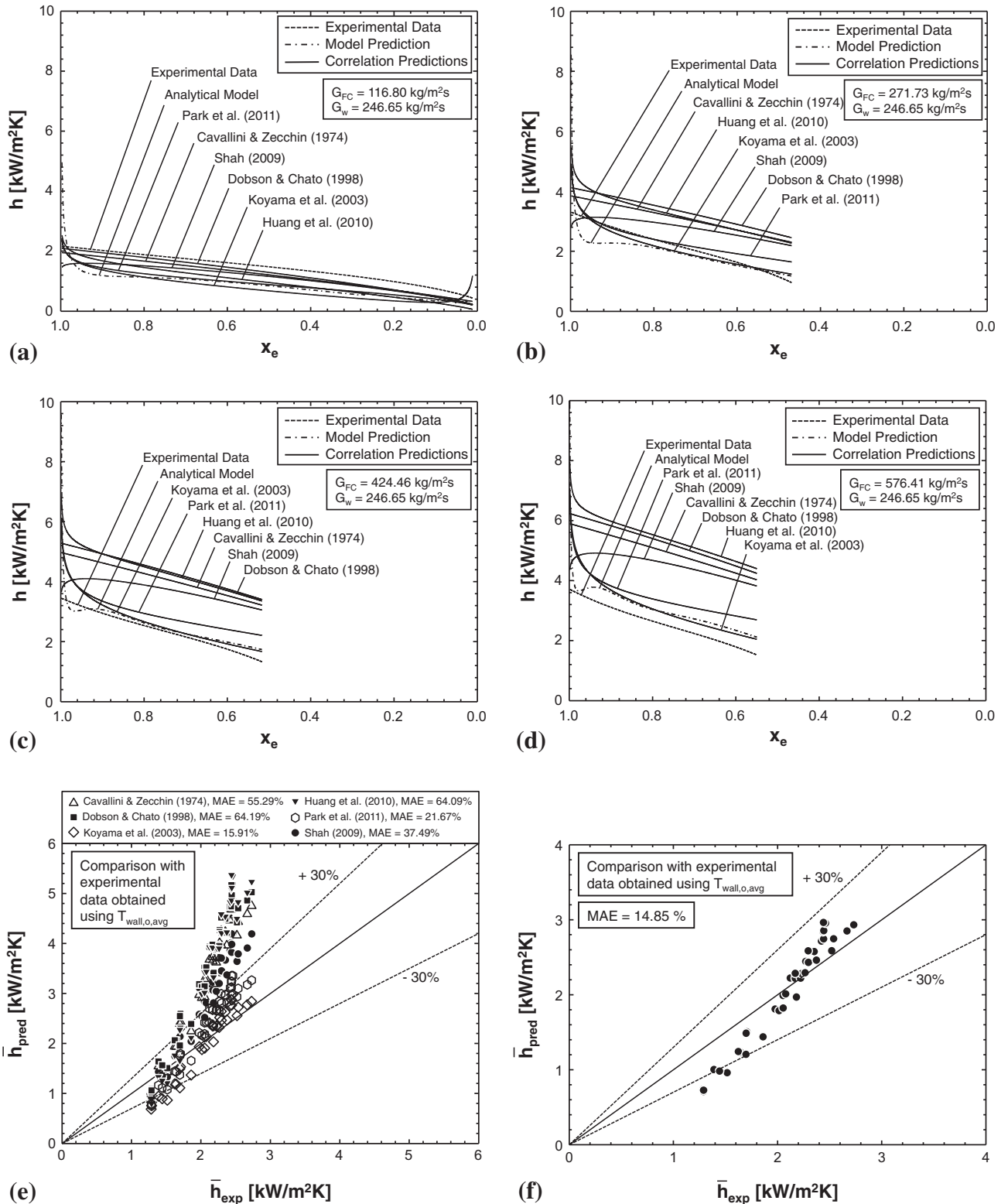


Fig. 11. Comparison of quality dependence of experimentally-determined local condensation heat transfer coefficient with predictions of the annular flow model and prior correlations for (a) $G_{FC} = 116.80$ kg/m² s, (b) $G_{FC} = 271.73$ kg/m² s, (c) $G_{FC} = 424.46$ kg/m² s, and (d) $G_{FC} = 576.41$ kg/m² s. Comparison of experimentally-determined average condensation heat transfer coefficient with predictions of (e) prior correlations and (f) the annular flow model.

and all six correlations, but with differences near $x_e = 1$. The model and three of the correlations based on the Lockhart–Martinelli parameter, X_{tt} , (Koyama et al. [50], Huang et al. [51] and Park et al. [52]) show a sharp decrease in h near $x_e = 1$, where the liquid film is the thinnest. On the other hand, the correlations of Cavallini and Zecchin [49] and Shah [27], which do not rely on

the Lockhart–Martinelli parameter, do not predict the sharp upstream decrease. In fact, the Shah correlation shows h increasing in the same region. Despite its dependence on the Lockhart–Martinelli parameter, X_{tt} , the correlation of Dobson and Chato [36] does not predict the sharp decrease near $x_e = 1$ because of its weak dependence on X_{tt} . And, while the experimentally-determined h

Table 6
Condensation heat transfer correlations.

Author(s)	Correlation	Remarks
Cavallini and Zecchin [49]	$\frac{hD_h}{k_f} = 0.05 \left[Re_g \left(\frac{\mu_g}{\mu_f} \right) \left(\frac{\rho_f}{\rho_g} \right)^{0.5} + Re_f \right] Pr_f^{0.33}$	x is substituted with x_e in comparison
Shah [27]	$\frac{hD_h}{k_f} = 0.023 Re_{fo}^{0.8} Pr_f^{0.4} \left(\frac{\mu_f}{14\mu_g} \right)^n \left[(1-x)^{0.8} + \frac{3.8x^{0.76}(1-x)^{0.04}}{Pr_R^{0.38}} \right]$ for $J_g \geq 0.98(Z + 0.263)^{-0.62}$ $\frac{hD_h}{k_f} = 0.023 Re_{fo}^{0.8} Pr_f^{0.4} \left(\frac{\mu_f}{14\mu_g} \right)^n \left[(1-x)^{0.8} + \frac{3.8x^{0.76}(1-x)^{0.04}}{Pr_R^{0.38}} \right] + 1.32 Re_f^{-1/3} \left[\frac{\rho_f(\rho_f - \rho_g)gk_f^2}{\mu_f^2} \right]^{1/3}$ for $J_g < 0.98(Z + 0.263)^{-0.62}$	$n = 0.0058 + 0.557 Pr_R$ $J_g = \frac{uG}{(gD_h \rho_g (\rho_f - \rho_g))^{0.5}}$ $Z = \left(\frac{1}{x} - 1 \right)^{0.8} Pr_R^{0.4}$
Dobson and Chato [36]	$\frac{hD_h}{k_f} = 0.023 Re_f^{0.8} Pr_f^{0.4} \left[1 + \frac{2.22}{X_{tt}^{0.69}} \right]$	x is substituted with x_e in comparison
Koyama et al. [50]	$\frac{hD_h}{k_f} = 0.0152 \left(1 + 0.6 Pr_f^{0.8} \right) \left(\frac{\phi_g}{X_{tt}} \right) Re_f^{0.77}$	$\phi_g = 1 + 21(1 - e^{-0.319D_h})X_{tt} + X_{tt}^2$ x is substituted with x_e in comparison
Huang et al. [51]	$\frac{hD_h}{k_f} = 0.0152 \left(-0.33 + 0.83 Pr_f^{0.8} \right) \left(\frac{\phi_g}{X_{tt}} \right) Re_f^{0.77}$	$\phi_g = 1 + 0.5 \left(\frac{G}{\sqrt{gD_h \rho_g (\rho_f - \rho_g)}} \right)^{0.75} X_{tt}^{0.35}$
Park et al. [52]	$\frac{hD_h}{k_f} = 0.0055 Re_f^{0.7} Pr_f^{1.37} \frac{\phi_g}{X_{tt}}$	$\phi_g^2 = 1 + 13.17 \left(\frac{\rho_g}{\rho_f} \right)^{0.17} \left(1 - \exp(-0.6\sqrt{Bo}) \right) X_{tt} + X_{tt}^2$

$$Re_g = \frac{Gx D_h}{\mu_g}, \quad Re_f = \frac{G(1-x)D_h}{\mu_f}, \quad Re_{fo} = \frac{GD_h}{\mu_f}, \quad X_{tt} = \left(\frac{1-x}{x} \right)^{0.9} \left(\frac{\rho_g}{\rho_f} \right)^{0.5} \left(\frac{\mu_f}{\mu_g} \right)^{0.1}, \quad Pr_R = \frac{P}{P_{crit}}, \quad Bo = \frac{g(\rho_f - \rho_g)D_h^2}{\sigma}$$

does not display the expected sharp decrease, this may be the result of the film being initiated in a more gradual manner rather than abruptly at $x_e = 1$ as discussed earlier in conjunction with Fig. 7. Despite the differences near $x_e = 1$, the annular model and all six correlations provide fairly good predictions of the data in terms of overall magnitude and trend with decreasing x_e .

Fig. 11(a) shows the model and all six correlations underpredict the data for $G_{FC} = 116.80 \text{ kg/m}^2 \text{ s}$. Fig. 11(b) shows the annular model and correlation by Koyama et al. underpredict the data, while the other correlations overpredict for $G_{FC} = 271.73 \text{ kg/m}^2 \text{ s}$. Fig. 11(c) and (d) shows the model and all the correlations overpredict the data for $G_{FC} = 424.46$ and $576.41 \text{ kg/m}^2 \text{ s}$, respectively.

5.4. Predictions of Average Condensation Heat Transfer Coefficient

Fig. 11(e) and (f) compares the experimentally-determined average heat transfer coefficient, \bar{h} , to predictions of the aforementioned six correlations and the annular model, respectively. Here, the heat transfer coefficient is averaged over the two-phase region only, excluding the short superheated region neat the inlet. The comparisons shown include data corresponding to all flow regimes, but exclude data for the six sets of operating conditions associated with subcooled liquid exit conditions. The data are based on the average outer wall temperature.

Fig. 11(e) shows the correlations predict the data with good to fair accuracy with mean absolute errors (MAEs) ranging from 15.91% to 64.19%, where $MAE = (1/N) \sum |(\bar{h}_{pred} - \bar{h}_{exp})/\bar{h}_{exp}|$. Overall, the correlations underpredict the data in the lower \bar{h} range and overpredict in the high \bar{h} range, with the correlation by Koyama et al. [50] yielding the best prediction, with the lowest MAE of 15.91% based on average outer wall temperature.

The model predictions in Fig. 11(f) show a general trend similar to that of the six correlations, but with far better agreement. The underprediction of data by the model in the lower \bar{h} range can be explained by the low FC-72 mass velocities in this range yielding appreciable gravity influence, which is not addressed in the model. On the other hand, overprediction of the data in the higher \bar{h} range may be related to interfacial waves, which, again, are not addressed in the model. Interfacial waves can influence annular condensation in several ways, by increasing interfacial area, altering turbulence within the film, and causing fluctuations in film thickness with the wave peaks moving faster than the thinner substrate. Nonetheless, with a MAE of 14.85%, the model provides good predictions of the data.

Aside from the need to address the influence of gravity for low mass velocities, it is recommended that future models incorporate the influence of interfacial waves. This important influence is prevalent in several two-phase flow configurations, including gravity-driven adiabatic films [53–56], sensibly heated films [57], evaporating films [58], and even in near critical heat flux flow boiling [59,60]. Further research is required to statistically characterize film thickness variations [53–56,61], as well as measure the influence of waves on velocity profile across the film [55,56].

6. Conclusions

This study explores condensation of FC-72 in a circular horizontal tube with the aid of both detailed heat transfer measurements and high-speed video motion analysis. Using a condensation module specifically designed for flow visualization, dominant condensation flow regimes are identified for different combination of mass velocities of FC-72 and cooling water. A separate test module specifically developed for acquisition of detailed heat transfer data is used to explore axial and circumferential variations of the condensation heat transfer coefficient. The heat transfer data are compared to predictions of both prior correlations and a control-volume-based annular flow model. Key findings from the study are as follows:

- (1) Four condensation regimes are identified, which, in order of increasing FC-72 mass velocity and decreasing gravity effects are *stratified*, *stratified-wavy*, *wavy-annular with gravity influence*, and *wavy-annular without gravity influence*. In the latter regime, which is achieved at high FC-72 mass velocities, motion of the annular film is dominated by vapor shear with no apparent gravity effects.
- (2) Using four different types of flow regime maps, transitions between the different regimes are compared to predictions of prior transition correlations. These correlations show fair agreement with the present flow regime data. New relations are also derived, which show better accuracy in predicting the regime transitions.
- (3) The effects of gravity are reflected in differences in the heat transfer coefficients determined from thermocouples inserted on the top versus bottom of the condensation tube. These differences are more pronounced for the *stratified* and *stratified-wavy* regimes. The heat transfer coefficient is highest near the inlet, where quality is near unity and the film

thinnest, and decreases gradually along the condensation length because of axial thickening of the liquid film. The heat transfer coefficient increases with increasing mass velocity of FC-72, which both increases interfacial shear and decreases film thickness.

- (4) The experimental data of both the local and average condensation heat transfer coefficients show fair to good agreement with predictions of prior and popular correlations. But superior predictions in both trend and magnitude are achieved with the annular flow model. A key advantage of the model is the ability to track detailed axial variations of film thickness, interfacial shear, and both liquid and vapor Reynolds numbers.

Conflict of interest

None declared.

Acknowledgment

The authors are grateful for the partial support for this project from the National Aeronautics and Space Administration (NASA) under Grant no. NNX13AB01G.

References

- [1] I. Mudawar, Two-phase micro-channel heat sinks: theory, applications and limitations, *J. Electron. Packag.* – Trans. ASME 133 (2011) 041002-2.
- [2] P.J. Marto, V.J. Lepere, Pool boiling heat transfer from enhanced surfaces to dielectric fluids, *J. Heat Transfer* – Trans. ASME 104 (1982) 292–299.
- [3] T.M. Anderson, I. Mudawar, Microelectronic cooling by enhanced pool boiling of a dielectric fluorocarbon liquid, *J. Heat Transfer* – Trans. ASME 111 (1989) 752–759.
- [4] I. Mudawar, A.H. Howard, C.O. Gersey, An analytical model for near-saturated pool boiling CHF on vertical surfaces, *Int. J. Heat Mass Transfer* 40 (1997) 2327–2339.
- [5] D.E. Maddox, I. Mudawar, Critical heat flux in subcooled flow boiling of fluorocarbon liquid on a simulated electronic chip in a rectangular channel, *Int. J. Heat Mass Transfer* 32 (1989) 379–394.
- [6] T.C. Willingham, I. Mudawar, Forced-convection boiling and critical heat flux from a linear array of discrete heat sources, *Int. J. Heat Mass Transfer* 35 (1992) 2879–2890.
- [7] H.J. Lee, S.Y. Lee, Heat transfer correlation for boiling flows in small rectangular horizontal channels with low aspect ratios, *Int. J. Multiphase Flow* 27 (2001) 2043–2062.
- [8] Y. Katto, M. Kunihiro, Study of the mechanism of burn-out in boiling system of high burn-out heat flux, *Bull. JSME* 16 (1973) 1357–1366.
- [9] M. Monde, T. Inoue, Critical heat flux in saturated forced convective boiling on a heated disk with multiple impinging jets, *J. Heat Transfer* – Trans. ASME 113 (1991) 722–727.
- [10] D.C. Wadsworth, I. Mudawar, Enhancement of single-phase heat transfer and critical heat flux from an ultra-high-flux-source to a rectangular impinging jet of dielectric liquid, *J. Heat Transfer* – Trans. ASME 114 (1992) 764–768.
- [11] M.E. Johns, I. Mudawar, An ultra-high power two-phase jet-impingement avionic clamshell module, *J. Electron. Packag.* – Trans. ASME 118 (1996) 264–270.
- [12] S. Toda, A study in mist cooling (1st report: investigation of mist cooling), *Trans. JSME* 38 (1972) 581–588.
- [13] L. Lin, R. Ponnappan, Heat transfer characteristics of spray cooling in a closed loop, *Int. J. Heat Mass Transfer* 46 (2003) 3737–3746.
- [14] J.R. Rybicki, I. Mudawar, Single-phase and two-phase cooling characteristics of upward-facing and downward-facing sprays, *Int. J. Heat Mass Transfer* 49 (2006) 5–16.
- [15] M. Visaria, I. Mudawar, Theoretical and experimental study of the effects of spray orientation on two-phase spray cooling and critical heat flux, *Int. J. Heat Mass Transfer* 51 (2008) 2398–2410.
- [16] W. Nakayama, T. Nakajima, S. Hirasawa, Heat sink studs having enhanced boiling surfaces for cooling of microelectronic components, ASME Paper 84-WA/HT-89 (1984).
- [17] R.L. Webb, The evolution of enhanced surface geometries for nucleate boiling, *Heat Transfer Eng.* 2 (1981) 46–69.
- [18] V. Khanikar, I. Mudawar, T. Fisher, Effects of carbon nanotube coating on flow boiling in a micro-channel, *Int. J. Heat Mass Transfer* 52 (2009) 3805–3817.
- [19] M.K. Sung, I. Mudawar, Experimental and numerical investigation of single-phase heat transfer using a hybrid jet-impingement/micro-channel cooling scheme, *Int. J. Heat Mass Transfer* 49 (2006) 682–694.
- [20] S.M. Kim, J. Kim, I. Mudawar, Flow condensation in parallel micro-channels-Part 1: experimental results and assessment of pressure drop correlations, *Int. J. Heat Mass Transfer* 55 (2012) 971–983.
- [21] J.M. Mandhane, G.A. Gregory, K. Aziz, A flow pattern map for gas-liquid flow in horizontal pipes, *Int. J. Multiphase Flow* 1 (1974) 537–553.
- [22] G. Breber, J. Palen, J. Taborek, Prediction of horizontal tube-size condensation of pure components using flow regime criteria, *J. Heat Transfer* – Trans. ASME 102 (1980) 471–476.
- [23] H.M. Soliman, On the annular-to-wavy flow pattern transition during condensation inside horizontal tubes, *Can. J. Chem. Eng.* 60 (1982) 475–481.
- [24] H.M. Soliman, The mist-annular transition during condensation and its influence on the heat transfer mechanism, *Int. J. Multiphase Flow* 12 (1986) 277–288.
- [25] Q. Chen, R.S. Amano, M. Xin, Experimental study of flow patterns and regimes of condensation in horizontal three-dimensional micro-fin tubes, *Int. J. Heat Mass Transfer* 43 (2006) 201–206.
- [26] S.M. Kim, I. Mudawar, Flow condensation in parallel micro-channels. Part 2: heat transfer results and correlation technique, *Int. J. Heat Mass Transfer* 55 (2012) 984–994.
- [27] M.M. Shah, An improved and extended general correlation for heat transfer during condensation in plain tubes, *HVAC&R Res.* 15 (2009) 889–913.
- [28] Y.Y. Yan, T.F. Lin, Condensation heat transfer and pressure drop of refrigerant R-134a in a small pipe, *Int. J. Heat Mass Transfer* 42 (1999) 697–708.
- [29] W.-W. Wang, T.D. Radcliff, R.N. Christensen, A condensation heat transfer correlation for millimeter-scale tubing with flow regime transition, *Exp. Therm. Fluid Sci.* 26 (2002) 473–485.
- [30] N.H. Kim, J.P. Cho, J.O. Kim, B. Youn, Condensation heat transfer of R-22 and R-410A in flat aluminum multi-channel tubes with or without micro-fins, *Int. J. Refrig.* 26 (2003) 830–839.
- [31] S.M. Kim, I. Mudawar, Universal approach to predicting two-phase frictional pressure drop for adiabatic and condensing mini/micro-channel flows, *Int. J. Heat Mass Transfer* 55 (2012) 3246–3261.
- [32] S.M. Kim, I. Mudawar, Universal approach to predicting heat transfer coefficient for condensing mini/micro-channel flow, *Int. J. Heat Mass Transfer* 56 (2013) 238–250.
- [33] I. Park, S.M. Kim, I. Mudawar, Experimental measurement and modeling of downflow condensation in a circular tube, *Int. J. Heat Mass Transfer* 57 (2013) 567–581.
- [34] H. Haraguchi, S. Koyama, T. Fujii, Condensation of refrigerants HCFC 22, HFC 134a and HCFC 123 in a horizontal smooth tube (2nd report, proposals of empirical expressions for local heat transfer coefficient), *Trans. JSME* 60 (1994) 2111–2116.
- [35] A. Singh, M.M. Ohadi, S.V. Dessiatoun, Empirical modeling of stratified-wavy flow condensation heat transfer in smooth horizontal tubes, *ASHRAE Trans.* 102 (1996) 596–606.
- [36] M.K. Dobson, J.C. Chato, Condensation in smooth horizontal tubes, *J. Heat Transfer* – Trans. ASME 120 (1998) 193–213.
- [37] R.G. Sardesai, R.G. Owen, D.J. Pulling, Flow regimes for condensation of a vapour inside a horizontal tube, *Chem. Eng. Sci.* 36 (1981) 1173–1180.
- [38] A. Cavallini, G. Censi, D.D. Col, L. Doretti, G.A. Longo, L. Rossetto, Condensation of halogenated refrigerants inside smooth tubes, *HVAC&R Res.* 8 (2002) 429–451.
- [39] H. Lee, I. Mudawar, M.M. Hasan, Flow condensation in horizontal tubes, *Int. J. Heat Mass Transfer* 66 (2013) 31–45.
- [40] I. Park, I. Mudawar, Climbing film, flooding and falling film behavior in upflow condensation in tubes, *Int. J. Heat Mass Transfer* 65 (2013) 44–61.
- [41] H. Lee, I. Mudawar, M.M. Hasan, Experimental and theoretical investigation of annular flow condensation in microgravity, *Int. J. Heat Mass Transfer* 61 (2013) 293–309.
- [42] R.K. Shah, A.L. London, *Laminar Flow Forced Convection in Ducts: A Source Book for Compact Heat Exchanger Analytical Data*, Academic Press, New York, 1978.
- [43] G.B. Wallis, *One-dimensional Two-phase Flow*, McGraw-Hill, New York, 1969.
- [44] S.M. Kim, I. Mudawar, Theoretical model for annular flow condensation in rectangular micro-channels, *Int. J. Heat Mass Transfer* 55 (2012) 958–970.
- [45] I. Mudawar, M.A. El-Masri, Momentum and heat transfer across freely-falling turbulent liquid films, *Int. J. Multiphase Flow* 12 (1986) 771–790.
- [46] H. Ueda, R. Moller, S. Komori, T. Mizushima, Eddy diffusivity near the free surface of open channel flow, *Int. J. Heat Mass Transfer* 20 (1977) 1127–1136.
- [47] W.M. Kays, Heat-transfer to transpired turbulent boundary-layer, *Int. J. Heat Mass Transfer* 15 (1972) 1023–1044.
- [48] W.M. Kays, M.E. Crawford, *Convective Heat and Mass Transfer*, second ed., McGraw-Hill, New York, 1980.
- [49] A. Cavallini, R. Zecchin, A dimensionless correlation for heat transfer in forced convection condensation, in: *Proc. 5th Int. Heat Transfer Conf.* vol. 3 (1974) pp. 309–313, Tokyo, Japan.
- [50] S. Koyama, K. Kuwahara, K. Nakashita, K. Yamamoto, An experimental study on condensation of refrigerant R134a in a multi-port extruded tube, *Int. J. Refrig.* 24 (2003) 425–432.
- [51] X. Huang, G. Ding, H. Hu, Y. Zhu, H. Peng, Y. Gao, B. Deng, Influence of oil on flow condensation heat transfer of R410A inside 4.18 mm and 1.6 mm inner diameter horizontal smooth tubes, *Int. J. Refrig.* 33 (2010) 158–169.
- [52] J.E. Park, F. Vakili-Farahani, L. Consolini, J.R. Thome, Experimental study on condensation heat transfer in vertical minichannels for new refrigerant R1234ze(E) versus R134a and R236fa, *Exp. Therm. Fluid Sci.* 35 (2011) 442–454.

- [53] T.H. Lyu, I. Mudawar, Statistical investigation of the relationship between interfacial waviness and sensible heat transfer to a falling liquid film, *Int. J. Heat Mass Transfer* 34 (1991) 1451–1464.
- [54] T.H. Lyu, I. Mudawar, Determination of wave-induced fluctuations of wall temperature and convective heat transfer coefficient in the heating of a turbulent falling liquid film, *Int. J. Heat Mass Transfer* 34 (1991) 2521–2534.
- [55] I. Mudawar, R.A. Houpt, Mass and momentum transport in falling liquid films laminarized at relatively high Reynolds numbers, *Int. J. Heat Mass Transfer* 36 (1993) 3437–3448.
- [56] I. Mudawar, R.A. Houpt, Measurement of mass and momentum transport in wavy-laminar falling liquid films, *Int. J. Heat Mass Transfer* 36 (1993) 4151–4162.
- [57] J.A. Shmerler, I. Mudawar, Local heat transfer coefficient in wavy free-falling turbulent liquid films undergoing uniform sensible heating, *Int. J. Heat Mass Transfer* 31 (1988) 67–77.
- [58] J.A. Shmerler, I. Mudawar, Local evaporative heat transfer coefficient in turbulent free-falling liquid films, *Int. J. Heat Mass Transfer* 31 (1988) 731–742.
- [59] J.C. Sturgis, I. Mudawar, Critical heat flux in a long, rectangular channel subjected to onesided heating – I. Flow visualization, *Int. J. Heat Mass Transfer* 42 (1999) 1835–1847.
- [60] J.C. Sturgis, I. Mudawar, Critical heat flux in a long, rectangular channel subjected to onesided heating – II. Analysis of critical heat flux data, *Int. J. Heat Mass Transfer* 42 (1999) 1849–1862.
- [61] J.E. Koskie, I. Mudawar, W.G. Tiederman, Parallel-wire probes for measurement of thick liquid films, *Int. J. Multiphase Flow* 15 (1989) 521–530.